HIGH FIELD TRANSPORT PHENOMENA IN WIDE BANDGAP SEMICONDUCTORS

A THESIS
SUBMITTED TO THE DEPARTMENT OF PHYSICS
AND THE INSTITUTE OF ENGINEERING AND SCIENCE
OF BILKENT UNIVERSITY
IN PARTIAL FULFILLMENT OF THE REQUIREMENTS
FOR THE DEGREE OF
MASTER OF SCIENCE

By
Cem Sevik
September, 2003

I certify that I have read this thesis and that in my opinion it is fully adequate, in scope and in quality, as a thesis for the degree of Master of Science.

Assist. Prof. Dr. Ceyhun Bulutay (Advisor)

I certify that I have read this thesis and that in my opinion it is fully adequate, in scope and in quality, as a thesis for the degree of Master of Science.

Prof. Dr. Ekmel Özbay

I certify that I have read this thesis and that in my opinion it is fully adequate, in scope and in quality, as a thesis for the degree of Master of Science.

Assoc. Prof. Dr. Cengiz Beşikçi

Approved for the Institute of Engineering and Science:

Prof. Dr. Mehmet B. Baray
Director of the Institute Engineering and Science

ABSTRACT

HIGH FIELD TRANSPORT PHENOMENA IN WIDE BANDGAP SEMICONDUCTORS

Cem Sevik
M.S. in Physics
Supervisor: Assist. Prof. Dr. Ceyhun Bulutay
September, 2003

The Ensemble Monte Carlo (EMC) method is widely used in the field of computational electronics related to the simulation of the state of the art devices. Using this technique our specific intention is to scrutinize the high-field transport phenomena in wide bandgap semiconductors (Such as GaN, AlGaN and AlN). For this purpose, we have developed an EMC-based computer code. After a brief introduction to our methodology, we present detailed analysis of three different types of devices, operating under high-field conditions, namely, unipolar n-type structures, avalanche photodiodes (APD) and finally the Gunn diodes. As a test-bed for understanding impact ionization and hot electron effects in sub-micron sized GaN, AlN and their ternary alloys, an n^+-n-n^+ channel device is employed having a 0.1 μm-thick n region. The time evolution of the electron density along the device is seen to display oscillations in the unintentionally doped n-region, until steady state is established. The fermionic degeneracy effects are observed to be operational especially at high fields within the anode n^+-region. For $Al_xGa_{1-x}N$-based systems, it can be noted that due to alloy scattering, carriers cannot acquire the velocities attained by the GaN and AlN counterparts. Next, multiplication and temporal response characteristics under a picosecond pulsed optical illumination of p^+-n-n^+ GaN and n-type Schottky $Al_{0.4}Ga_{0.6}N$ APDs are analyzed. For the GaN APD, our simulations can reasonably reproduce the available measured data without any fitting parameters. In the case of AlGaN, the choice of a Schottky contact APD is seen to improve drastically the field confinement resulting in satisfactory gain characteristics. Moreover, alloy scattering is seen to further slow down the temporal response while displacing the gain threshold to higher fields. Finally, the dynamics of large-amplitude Gunn domain oscillations from 120 GHz to 650 GHz are studied in detail by means of extensive EMC simulations. The basic operation is checked under both impressed single-tone sinusoidal bias and external tank circuit conditions. The width of the doping-notch is observed to

enhance higher harmonic efficiency at the expense of the fundamental frequency up to a critical value, beyond which sustained Gunn oscillations are ceased. The degeneracy effects due to the Pauli Exclusion principle and the impact ionization are also considered but observed to have negligible effect within the realistic operational bounds. Finally, the effects of lattice temperature, channel doping and DC bias on the RF conversion efficiency are investigated.

Keywords: High field transport, Ensemble Monte Carlo technique, Avalanche photodiodes, Gunn diodes, Unipolar devices.

ÖZET

GENİŞ BANT ARALIKLI YARIİLETKENLERDE YÜKSEK ELEKTRİK ALANI ALTINDA İLETİM OLAYLARI

Cem Sevik
Fizik, Yüksek Lisans
Tez Yöneticsi: Yard. Doç. Dr. Ceyhun Bulutay
Eylül, 2003

Toplu Monte Carlo (TMC) yöntemi en modern aygıtların benzetimi maksadıyla, geniş bant aralıklı yarı iletkenlerde yüksek elektrik alanı altında iletkenliği incelemek için kullanılmaktadır. Bizim amacımız, bu yöntemi kullanarak geniş bant aralıklı yarı iletkenlerde (GaN, AlGaN and AlN gibi) yüksek elektrik alanı altında iletkenliği geniş bir şekilde incelemektir. Bu amaca uygun olarak, ilk önce TMC-tabanlı bir bilgisayar yazılımı geliştirilmiştir. Yaklaşımımız hakkında kısa bir girişten sonra yüksek elektrik alanı altında calışabilen üç farklı aygıt incelenmiştir; tek kutuplu n-tipi yapı, çığ fotoalgılayıcıları ve Gunn diyotları. Darbe iyonizasyonu ve ilgili sıcak-elektron etkilerini incelemek için 0.1 μm genişliğinde n-katkılı bölge içeren $(n^+ - n - n^+)$ yapısı kullanılmıştır. n-katkılı bölge içerisinde elektron yoğunluğunun durağan-hale ulaşıncaya kadar zamana göre salınım yaptığı görülmüştür. Ayrıca yüksek elektrik alanı altında fermiyonik çakışıklık etkilerinin özellikle n^+-katkılı bölgede baskın olduğu gözlenmiştir. AlGaN yapısında elektronların hızının GaN ve AlN yapılarındaki elektronların hızlarının arasında bir değerde olmadığı ve bunun sebebinin de baskın alaşım saçınımının olduğu saptanmıştır. Daha sonra, GaN ve n-tipi Schottky AlGaN çığ fotoalgılayıcılarının çarpma ve pico-saniyelik aydınlatma altında zamana göre tepki karakteristiği analiz edilmiştir. GaN foto algılayıcıları konusunda, bizim benzetimlerimiz, hiç bir oturtma parametresine gerek kalmadan mevcut deneysel sonuçlarla makul bir uyum göstermektedir. AlGaN yapısında, yüksek kazanç sağlayan bölgedeki elektrik alanını yükseltmek için Schottky bağlantılı çığ fotoalgılayıcısı yapısının kullanılmasının uygun olduğu tesbit edilmiştir. Öte yandan, AlGaN yapısında, alaşım saçınımının, aygıtın zamana göre tepkisini yavaşlatığı ve kazanç eşiğini yüksek gerilimlere taşıdığı gözlenmiştir. Son olarak, 120 GHz´ten 650 GHz´e kadar geniş-genlikli Gunn salınımları TMC yöntemi ile

detaylı bir şekilde incelenmiştir. Gunn diyotların özellikleri hem zorunlu uygulanan tek-tonlu sinüs gerilimi altında hem de dış rezonans devresine bağlanarak kontrol edilmiştir. Katkılama çentiğinin genişliğinin yüksek harmoniklerdeki verimi, belirli bir kritik değere kadar olumlu etkilediği gözlenmiştir. Pauli dışarlama etkisinden kaynaklanan çakışıklık etkilerinin ve darbe iyonizasyonunun Gunn diyotun çalışmasında çok etkili olmadığı görülmüştür. En son olarak, örgü sıcaklığı, kanal katkılaması ve DC beslemesinin, RF dönüştürme verimi üzerindeki etkisi incelenmiştir.

Anahtar sözcükler: Yüksek elektrik alanı altında iletim, Toplu Monte Carlo yöntemi, Çığ fotoalgılayıcı, Gunn diyot, Tekkutuplu aygıtlar.

Acknowledgement

I would like to express my gratitude to my supervisor Assist. Prof. Dr. Ceyhun Bulutay for his instructive comments in the supervision of the thesis.

Contents

1 Introduction **1**

1.1 This work . . . 2

2 Monte Carlo charge transport simulation **4**

2.1 A typical MC program . . . 4

2.1.1 Definition of the physical system and simulation parameters 6

2.1.2 Initialization . . . 7

2.1.3 Free flight . . . 7

2.1.4 Identification of the scattering event . . . 10

2.1.5 Choice of state after scattering . . . 12

2.2 MC simulation and the Boltzman Transport Equation . . . 14

2.3 The evolution of the Bilkent EMC code . . . 15

3 Hot electron effects in *n*-type structures **17**

3.1 Computational details . . . 18

3.2 Alloy scattering . . . 19

3.3 Results 20

4 AlGaN solar-blind avalanche photodiodes 23

4.1 Computational details 24

4.2 Results 26

4.2.1 GaN APDs 26

4.2.2 Schottky contact-AlGaN APDs 28

5 Gunn oscillations in GaN channels 32

5.1 Basics 33

5.2 Motivation 35

5.3 Computational details 36

5.4 Results 37

5.4.1 The effect of notch width 38

5.4.2 The effect of lattice temperature 40

5.4.3 The effect of channel doping 41

5.4.4 The effect of DC operating point 42

5.4.5 Connecting to a tank circuit 43

5.5 Computational budget 44

6 Summary of the main findings 45

A Impact ionization and alloy scattering 52

A.1 Impact ionization 52

A.2 Alloy scattering 56

List of Figures

2.1 Flowchart of the typical MC Program. 5

2.2 (a)The path of the particle in wave-vector space. (b) The path of the particle in real space. 6

2.3 Total scattering rate versus energy for electrons in a model semiconductor. 9

2.4 Fractional contribution versus energy for five scattering processes. (1) Acoustic Deformation Potential, (2) Intervalley absorption, (3) Intervalley emission, (4) Ionized impurity, (5) self scattering. . . . 10

2.5 Illustration of the procedure for identifying a scattering event. . . 11

2.6 (a) Scattering event in the $(\hat{x}, \hat{y}, \hat{z})$ coordinate system. The incident momentum is $\mathbf{k}$ and the scattered momentum, $\mathbf{k}'$. (b) The same scattering event in the rotated coordinate system, $(\hat{x}_r, \hat{y}_r, \hat{z}_r)$ by an angle of ϕ about the $\hat{x} - axis$, then θ about the the $\hat{y} - axis$. In the rotated system the incident momentum is $\mathbf{k}_r$ and the scattered momentum $\mathbf{k}_r'$. 13

2.7 The empirical pseudopotential band structure of the GaN and AlN. 15

3.1 Structural schematic 18

3.2 Velocity distribution over the $n^+ - n - n^+$ channel under an applied bias of 20 V. 19

3.3 Electric field distribution over the $n^+ - n - n^+$ GaN channel at applied biases ranging from 5 V to 50 V. 20

3.4 Time evolution of the transient electron density profile over the $n^+ - n - n^+$ GaN channel under an applied bias of 50 V; steady state result is also shown, evaluated at 7.5 ps. 21

3.5 (a) Steady state density profile at a bias of 50 V, with and without the degeneracy effects included. (b) Energy distribution over the $n^+ - n - n^+$ GaN channel under an applied bias of 80 V, with and without impact ionization being included. 22

4.1 Structural details. 25

4.2 (a) Current gain of the GaN APD; EMC simulation (symbols) compared with measurements [23] (dotted). (b) Current gain of the $Al_{0.4}Ga_{0.6}N$ APD simulated using EMC with and without alloy scattering. Full lines in EMC curves are used to guide the eye. . . 26

4.3 Temporal response of the GaN and $Al_{0.4}Ga_{0.6}N$ (vertically shifted for clarity) APD to a 25 ps optical pulse, applied between the dashed lines. 28

4.4 Electric field distribution over (a) GaN (b) $Al_{0.4}Ga_{0.6}N$ APDs at several bias levels. 29

4.5 Average velocity distribution over (a) GaN (b) $Al_{0.4}Ga_{0.6}N$ APDs for electron (solid) and holes (dotted). 30

5.1 EMC simulation of the drift velocity versus field for bulk GaN at 300 K. 33

5.2 Equivalent circuit for a uniform piece of semiconductor. 34

5.3 Structural details. 36

5.4 (a) Typical charge density profiles for a 250 nm-notch device operating at the fundamental, second, third, fourth-harmonic modes, each respectively vertically up-shifted for clarity. (b) Time evolution of the electric field profile within one period of the Gunn oscillation at 2 ps intervals for the 250 nm-notch device. 38

5.5 Gunn diode efficiency versus frequency. (a) Effect of different doping-notch widths, while keeping the total active channel length fixed at 1.2 μm. (b) Effect of including the Pauli exclusion principle for the 250 nm-notch device. 39

5.6 RF conversion efficiency versus frequency for several lattice temperatures; 250 nm-notch device at 60 V bias is used. 40

5.7 RF conversion efficiency versus frequency for several channel dopings; 250 nm-notch device at 60 V bias is used. 41

5.8 RF conversion efficiency versus frequency for several DC bias voltages; 250 nm-notch device. 42

5.9 Current and voltage waveforms for a 150 nm-notch Gunn diode (a) under an imposed single-tone sinusoidal voltage, and (b) connected to an external tank circuit shown in the inset. 43

A.1 Electron II coefficient versus inverse electric field. Dotted lines indicate the results when alloy scattering is not included, after Jung [49]. 55

A.2 Electron II coefficient versus inverse electric field. Dotted lines indicate the results when alloy scattering is not included. The curves for $Al_{0.6}Ga_{0.4}N$ and $Al_{0.8}Ga_{0.2}N$ merge at higher fields. These results are obtained for a temperature of 300 K and an ionized impurity concentration of 10^{17} cm^{-3}. 56

A.3 Electron energy distribution for $Al_{0.4}Ga_{0.6}N$ at an electric field of 3.5 MV/cm, with (solid) and without (dotted) the alloy scattering. A temperature of 300 K and an ionized impurity concentration of 10^{17} cm^{-3} are considered 57

List of Tables

4.1 Fitted temporal response functions $\exp(-t^2/\tau_f^2)$ and $1 - \exp(-t^2/\tau_r^2)\cos(\omega_r t)$ for the GaN APD. 27

4.2 Fitted temporal response functions $\exp(-t/\tau_f)$ and $1-\exp(-t^2/\tau_r^2)$ for $Al_{0.4}Ga_{0.6}N$ APD under a reverse bias of 30 V. 30

A.1 Band edge analysis throughout the lowest two conduction bands of $Al_xGa_{1-x}N$ alloys: band edge energy, E, density of states effective mass, m^*, and non-parabolicity factor, α (other than the lowest valley, two-band $\vec{k} \cdot \vec{p}$ values are preferred). Equivalent valley multiplicities, N_v are included as well. Note that the ordering of the U and K valleys is interchanged at an aluminium mole fraction of 0.6. 53

A.2 A and K values in the electron II coefficient expression, $A \exp(-K/F)$, where, F is the electric field. A temperature of 300 K and an ionized impurity concentration of 10^{17} cm^{-3} are used. . 54

Chapter 1

Introduction

The wide band gap semiconductors, especially GaN, AlN and their ternary alloys, are of increasing importance in various applications from high frequency, high power amplifiers to blue and ultraviolet light emitters and detectors [1, 2]. Though these materials have much practical importance, they are still technologically immature. As a result, their high-field transport properties and hence the corresponding device potential are yet to be uncovered. Progress in assessing the device potential of the wide band gap semiconductor materials is impeded experimentally by the lack of sufficient device quality material which makes computational approaches quite valuable in this respect.

The high-field transport, on the other hand, is in general a tough problem [3], from both the mathematical and the physical points of view. In fact, the integro-differential equation, the Boltzmann transport equation, that describes the problem does not offer simple (or even complicated) analytical solutions except for very few cases, and these cases usually are not applicable to real systems. Furthermore, since transport quantities are derived from the averages over many physical processes whose relative importance is not known a priori, the formulation of reliable microscopic models for the physical system under investigation is difficult. When one moves from linear to nonlinear response conditions, the difficulties become even greater: the analytical solution of the Boltzmann transport equation without linearization with respect to the external force is a formidable

mathematical problem, which has resisted many attacks in the last few decades. In order to get any result, it is necessary to perform such drastic approximations that it is no longer clear whether the features of interest in the results are due to the microscopic model or to mathematical approximations.

From the foregoing it is understandable that, when two new numerical approaches to this problem, i.e., the Monte Carlo technique (Kurosawa, 1966) and the iterative technique (Budd, 1966), were presented at the Kyoto Semiconductor Conference in 1966, hot-electron physicists received the new proposals with great enthusiasm. It was in fact clear that, with the aid of modern large and fast computers, it would become possible to obtain exact numerical solutions of the Boltzmann equation for microscopic physical models of considerable complexity. These two techniques were soon developed to a high degree of refinement by Price (1968), Rees (1969), and Fawcett *et al.* (1970), and since then they have been widely used to obtain results for various situations in practically all materials of interest. The Monte Carlo method is by far the more popular of the two techniques mentioned above, because it is easier to use and more directly interpretable from the physical point of view.

The particular advantage of the Monte Carlo method is that it provides a first principles transport formulation based on the exact solution of the Boltzmann equation, limited only by the extent to which the underlying physics of the system is included. With these virtues, the ensemble Monte Carlo technique has become our workhorse to tackle challenging high-field transport phenomena in wide bandgap semiconductors, which are itemized in the following section.

1.1 This work

As a preliminary step in Chapter 3, we start with the high-field transport in sub-micron sized, n-doped unipolar structures. Our analysis includes the alloy scattering, impact ionization and degeneracy effects as well as the detailed transient time evolution of the electron density along the device. This part of the

thesis work has been published in the IEE Proceedings: Optoelectronics [4].

Next in Chapter 4, gain and temporal response characteristics of the GaN and $Al_{0.4}Ga_{0.6}N$ APDs are investigated. Especially the latter has technological importance for the solar-blind photodetection. Results for the $Al_{0.4}Ga_{0.6}N$ APDs are provided both with and without the alloy scattering. To the best of our knowledge, these simulations published in Applied Physics Letters [5] constitute the only available data in the literature for this device.

Finally in Chapter 5, GaN-based Gunn diodes which can be utilized as a solid-state high power millimeter wave oscillator are analyzed in detail. Particularly, we show that the doping-notch width can be adjusted to enhance more efficient RF conversion at higher harmonics than the fundamental frequency. The degeneracy and impact ionization effects are observed to be insignificant. The effects of channel doping, lattice temperature and the DC bias level are thoroughly studied. A part of this chapter has been presented in 13th International Conference on Non-equilibrium Carrier Dynamics in Semiconductors (Modena/Italy) and will be published in the journal, Semiconductor Science and Technology [8].

Chapter 2

Monte Carlo charge transport simulation

Much of our understanding of high-field transport in bulk semiconductors and in devices has been obtained through Monte Carlo (MC) simulation, so it is important to understand the basics of the method. Because it directly mimics the physics, an understanding of the technique is also useful for the insight it affords. One can find excellent resources on the MC technique [3, 6, 7, 10]; here, we only include a brief introduction for documentation purposes which can be skipped by those who feel familiar with the subject. Some details about the Bilkent EMC code is also provided at the end of this chapter.

2.1 A typical MC program

For the sake of simplicity we shall refer to the case of electrons in a simple semiconductor subject to an external electric field $\mathbf{E}$[1]. The simulation starts with electrons in given initial conditions with wave vector $\mathbf{k}_0$; then, the duration of the first free flight is chosen with a probability distribution determined by the scattering probabilities. During the free flight the external forces are made to act

[1]The contents of this section are not original and has been adopted from Lundstrom [6].

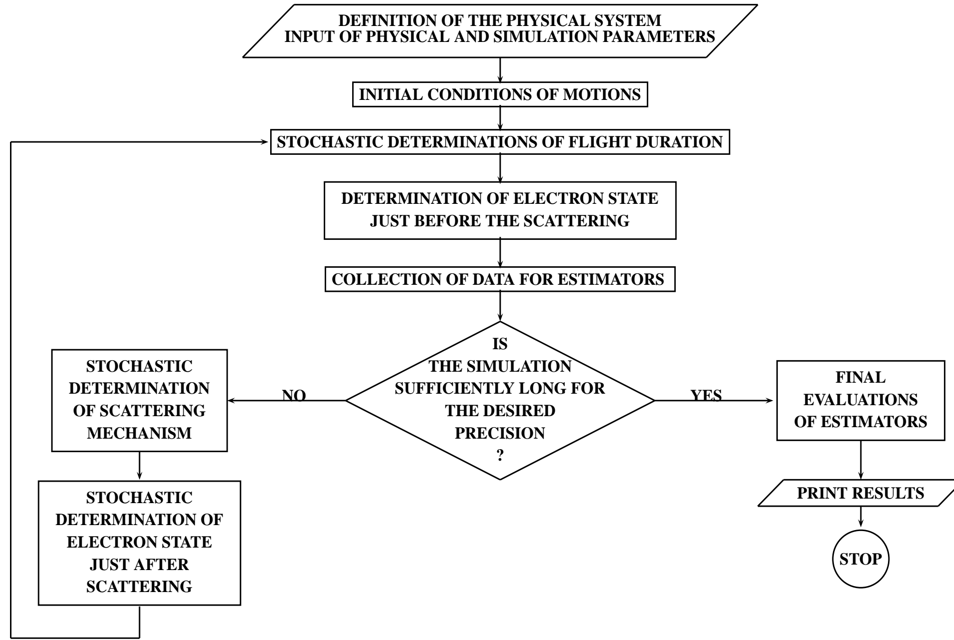

Figure 2.1: Flowchart of the typical MC Program.

according to the relation

$$\hbar \dot{\mathbf{k}} = e\mathbf{E}, \tag{2.1}$$

where $\mathbf{k}$ is the carrier wave vector, e its charge with its sign ($e < 0$ for electrons and $e > 0$ for holes), and $\hbar$ the Planck constant divided by 2π. In this part of the simulation all quantities of interest, velocity, energy, etc., are recorded. Then a scattering mechanism is chosen as responsible for the end of the free flight, according to the relative probabilities of all possible scattering mechanisms. From the differential cross section of this mechanism a new $\mathbf{k}$ state after scattering is determined which acts as the initial state of the new free flight, and the entire process is iteratively repeated. The results of the calculation become more and more precise as the simulation goes on, and the simulation ends when the quantities of interests are known with the desired precision. A simple way to determine the precision, that is, the statistical uncertainty, of transport quantities consists of dividing the entire history into a number of successive sub histories of equal time duration, and making a determination of a quantity of interest for each of them. We then determine the average value of each quantity and take its standard deviation as an estimate of its statistical uncertainty. Figure. 2.1 shows a

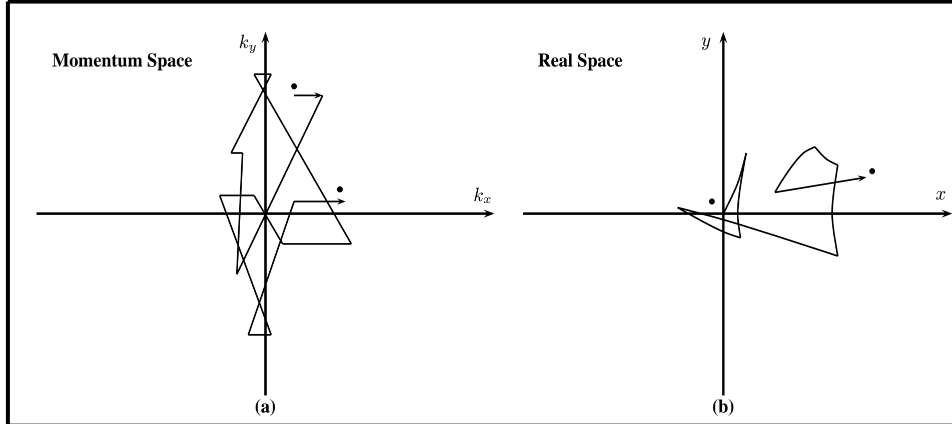

Figure 2.2: (a)The path of the particle in wave-vector space. (b) The path of the particle in real space.

flowchart of a simple MC program suited for the simulation of a stationary, homogeneous transport process. Figure. 2.2 illustrates the principles of the method by showing the simulation in momentum **k** space and real space.

2.1.1 Definition of the physical system and simulation parameters

The starting point of the program is the definition of the physical system of interest, including the parameters of the material and the values of physical quantities, such as lattice temperature T_0 and electric field. It is worth noting that, among the parameters that characterize the material, the least known, usually taken as adjustable parameters, are the coupling strengths describing the interactions of the electron with the lattice and/or extrinsic defects inside the crystal. At this level we also define the parameters that control the simulation, such as the duration of each sub history, the desired precision of the results, and so on. The next step in the program is tabulation of each scattering rate as a function of electron energy. This step will provide information on the maximum value of these functions, which will be useful for optimizing the efficiency of the simulation.

2.1.2 Initialization

Finally, all cumulative quantities must be put at zero in this preliminary part of the program. In the particular case of a very high electric field, if an energy of the order of $k_B T_0$ (k_B being the Boltzmann constant) is initially given to the electron, this energy will be much lower than the average energy in steady-state conditions, and during the transient it will increase towards its steady-state value.

The longer the simulation time, the less influence the initial conditions will have on the average results; however, in order to avoid the undesirable effects of an inappropriate initial choice and to obtain a better convergence, the elimination of the first part of the simulation from the statistics may be advantageous. The simulation start with charge density which cancel the background impurity dop-ing.

2.1.3 Free flight

After moving for a time, t, under the influence of a $\hat{x}$-directed electric field, the electron's momentum and position are obtained from Eqs. 2.1.

$$\mathbf{r}(t) = \mathbf{r}(0) + \int_0^t \upsilon(t^{'})dt^{'}. \tag{2.2}$$

We assume that the field, E_x, is nearly constant for the duration of the free flight. The first question to consider is: how long should the free flight continue - or what is the time of the next collision? The duration of the free flight is directly related to the scattering rate - the higher the scattering rate the shorter the average free flight.

Within our approximations, we may simulate the actual transport by introducing a probability density $P(t)$, where $P(t)dt$ is the joint probability that a carrier will both arrive at time t without scattering (after its last scattering event at $t = 0$), and then will actually suffer a scattering event at this time (i.e., within a time interval dt centered at t). The probability of actually scattering within this small time interval at time t may be written as $\Gamma[k(t)]dt$, where $\Gamma[k(t)]$ is the total

scattering rate of a carrier of wave vector $k(t)$. This scattering rate represents the sum of the contributions of each scattering process that can occur for a carrier of this wave vector (and energy). The explicit time dependence indicated is a result of the evolution of the wave vector under any accelerating electric (and magnetic) field. In terms of this total scattering rate, the probability that a carrier has not suffered a collision after time t is given by

$$\exp\left(-\int_0^t \Gamma[k(t^{'})]dt^{'}\right). \tag{2.3}$$

Thus, the probability of scattering within the time interval dt after a free flight time t, measured since the last scattering event, may be written as the joint probability

$$P(t)dt = \Gamma[k(t)]\exp\left(-\int_0^t \Gamma[k(t^{'})]dt^{'}\right)dt, \tag{2.4}$$

Random flight times may now be generated according to the probability density $P(t)$ by using, for example, the pseudo-random number generator available on nearly all modern computers and which yields random numbers in the range [0,1]. Using a simple, direct methodology, the random flight time is sampled from $P(t)$ according to the random number r as

$$r = \int_0^t P(t^{'})dt^{'}. \tag{2.5}$$

For this approach, it is essential that r is uniformly distributed through the unit interval, and the result t is the desired flight time. Using Eq. (2.4) in Eq. (2.5) yields

$$r = 1 - \exp\left(-\int_0^t \Gamma[k(t^{'})]dt^{'}\right). \tag{2.6}$$

Since 1 - r is statistically the same as r, this latter expression may be simplified as

$$-\ln(r) = \int_0^t \Gamma[k(t^{'})]dt^{'}. \tag{2.7}$$

The set of Eqs. (2.6) and (2.7) are the fundamental equations used to generate the random free flight for each carrier in the ensemble. If there is no accelerating field, the time dependence of the wave vector vanishes, and the integral is trivially evaluated. In the general case, however, this simplification is not possible, and it is expedient to resort to another trick. Here, one introduces a fictitious scattering process that has no effect on the carrier. This process is called *self-scattering*

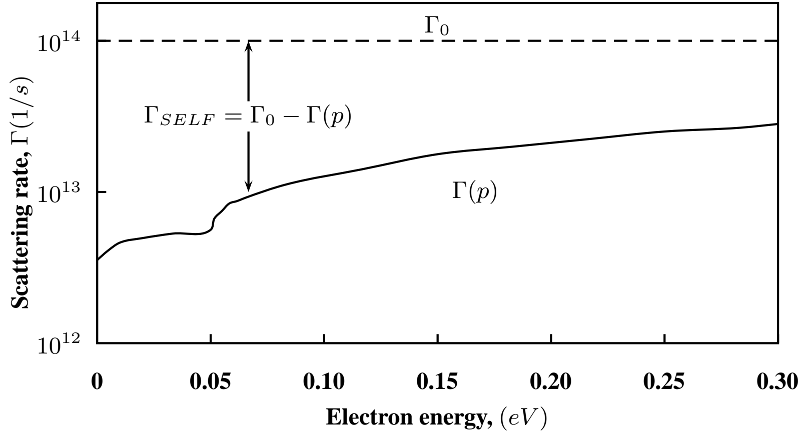

Figure 2.3: Total scattering rate versus energy for electrons in a model semiconductor.

(Fig. 2.3), and the energy and momentum of the carrier are unchanged under this process (Rees, 1969). However, we will assign an energy dependence to this process in just such a manner that the total scattering rate is a constant, as

$$\Gamma_{self}[k(t)] = \Gamma_0 - \Gamma[k(t)] = \Gamma_0 - \sum_i \Gamma_i[k(t)], \tag{2.8}$$

and the summation runs over all real scattering processes. Its introduction eases the evaluation of the free flight times, as now

$$t_c = -\frac{1}{\Gamma_0} \ln(r). \tag{2.9}$$

With the addition of self-scattering, the total scattering rate is constant, so Eq. (2.9) now applies, but we must be certain that the fictitious scattering mechanism introduced does not alter the problem. Real scattering events alter the carrier's momentum, but when a self-scattering event occurs we do not change the carrier's momentum. Self-scattering does not affect the carrier's trajectory - it simply makes the scattering rate constant so that Eq. (2.9) applies. When a free flight is terminated by a fictitious scattering event, a new random number is generated and the free flight continues.

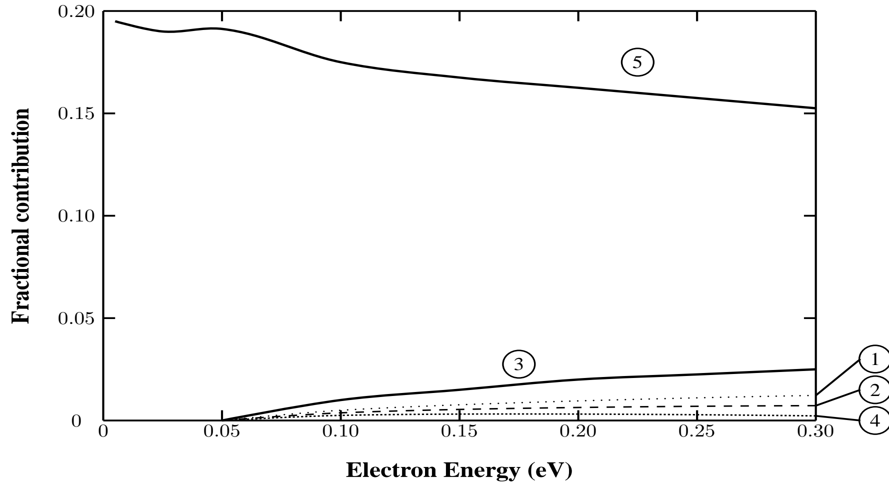

Figure 2.4: Fractional contribution versus energy for five scattering processes. (1) Acoustic Deformation Potential, (2) Intervalley absorption, (3) Intervalley emission, (4) Ionized impurity, (5) self scattering.

2.1.4 Identification of the scattering event

After selecting the duration of the free flight using the prescription, Eq. 2.9, the carrier's momentum, position, and energy are updated at time t_c^-. Collisions alter the carrier's momentum, but each mechanisms does so differently. To update the momentum at t_c^+, we must first identify the scattering event that terminated the free flight and determine whether it was real or fictitious.

The contribution of each individual scattering mechanism to the total scattering rate varies considerably with energy. Since we have now added a $(k+1)$th scattering mechanism, the contribution of self-scattering must also be included. For the real processes and for the fictitious process, we calculate the fractional contribution of all scattering mechanism (by using Eq. 2.8 for self scattering and mechanism specific formula for the others, we will see later) as seen in Fig. 2.4. Because the carrier's energy at the end of the free flight is known, the probabilities of the various events can be read directly from the figure. By adding up the various contributions in this order, we obtain the graph shown in Fig. 2.5.

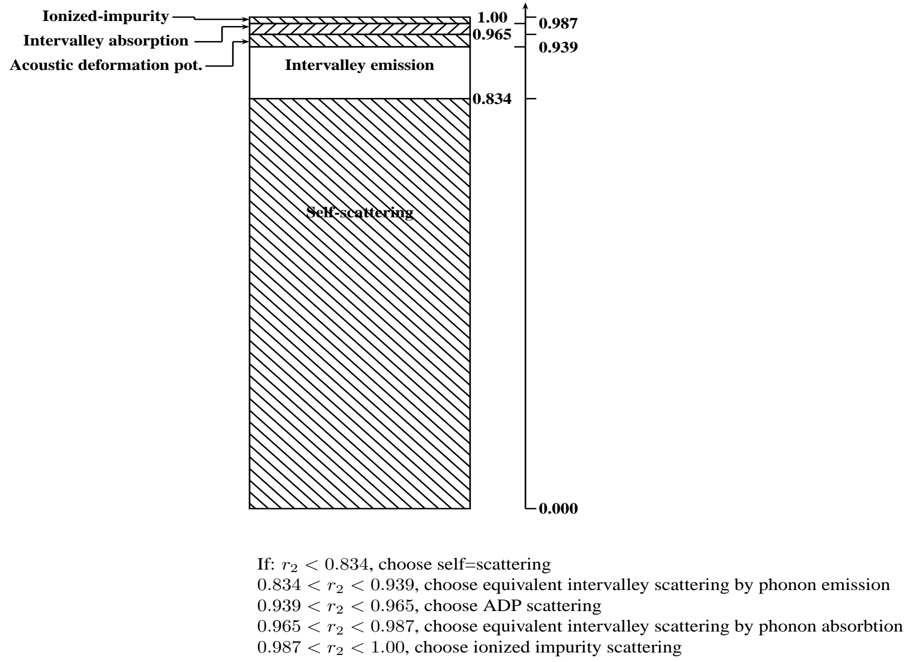

Figure 2.5: Illustration of the procedure for identifying a scattering event.

Selection of a random number, r_2, uniformly distributed from zero to one locates a region in the graph and identifies the scattering event.

The mathematical description of the identification procedure is to select mechanism l, if

$$\frac{\sum_{i=1}^{l-1} \frac{1}{\tau_i(p)}}{\Gamma_0} \leq r_2 < \frac{\sum_{i=1}^{l} \frac{1}{\tau_i(p)}}{\Gamma_0} \qquad l = 1, 2, 3, ...k + 1. \tag{2.10}$$

The procedure consists of determining the carrier's energy just before the collision, constructing a bar graph like that in Fig. 2.5, choosing a random number, r_2, and locating it within the bar graph to identify the scattering event.

2.1.5 Choice of state after scattering

Once the scattering mechanism that caused the end of the electron free flight has been determined, the new state after scattering of the electron, $k^{'}$ must be chosen as the final state of the scattering event. If the free flight ended with a self-scattering, $k^{'}$ must be taken as equal to k, the state before scattering. When, in contrast, a true scattering occurred, then $k^{'}$ must be generated, stochastically, according to the differential cross section of that particular mechanism.

For spherical, parabolic energy bands, the magnitude of the carrier's momentum just after scattering is

$$k(t_c^+) = k^{'} = \sqrt{2m^*[E(t_c^-) + \Delta E]}/\hbar, \tag{2.11}$$

where ΔE is the change in energy associated with the particular scattering event selected by random number r_2. For elastic scattering, $\Delta E = 0$, and for inelastic scattering it is typically a phonon energy. Because there is a unique ΔE associated with each scattering event, random number r_2 also determines the magnitude of the carrier's momentum after scattering, but to update the orientation of $\mathbf{k}$, two more random numbers must be selected.

When updating the orientation of $\mathbf{k}$, it is convenient to work in a coordinate system in which the $\hat{x}$ axis is directed along the initial momentum $\mathbf{k}$. The new coordinate system ($\hat{x}_r$, $\hat{y}_r$, $\hat{z}_r$) is obtained by rotating the ($\hat{x}$, $\hat{y}$, $\hat{z}$) system by an angle ϕ about the $\hat{x}$ axis, then θ about $\hat{y}$ as illustrated in Fig. 2.6. The probability that k_a lies between azimuthal angle β and $\beta + d\beta$ is found by evaluating

$$P(\beta)d\beta = \frac{d\beta \int_0^\infty \int_0^\pi S(k,k^{'}) \sin\alpha d\alpha k^{'2} dk^{'}}{\int_0^{2\pi} d\beta \int_0^\infty \int_0^\pi S(k,k^{'}) \sin\alpha d\alpha k^{'2} dk^{'}}. \tag{2.12}$$

Because this simple treatment of scattering makes the transition rate independent of β, the integration over β in the denominator can be performed directly, and

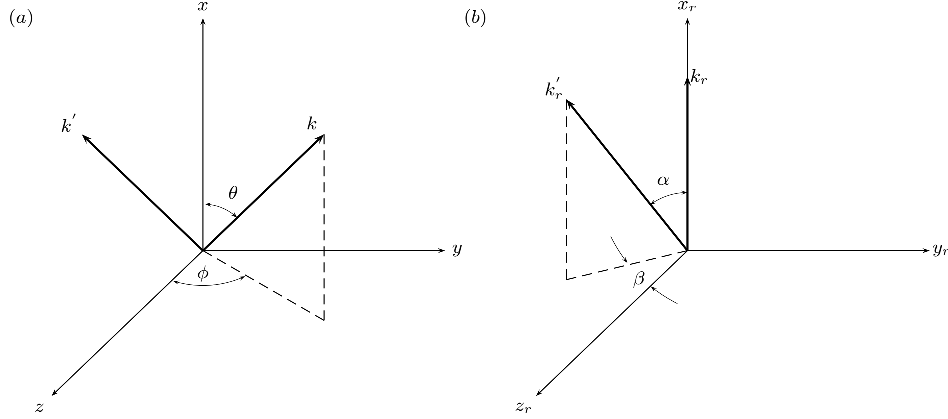

Figure 2.6: (a) Scattering event in the $(\hat{x}, \hat{y}, \hat{z})$ coordinate system. The incident momentum is $\mathbf{k}$ and the scattered momentum, $\mathbf{k}^{'}$. (b) The same scattering event in the rotated coordinate system, $(\hat{x}_r, \hat{y}_r, \hat{z}_r)$ by an angle of ϕ about the $\hat{x} - axis$, then θ about the the $\hat{y} - axis$. In the rotated system the incident momentum is $\mathbf{k}_r$ and the scattered momentum $\mathbf{k}_r^{'}$.

we find

$$P(\beta)d\beta = d\beta/2\pi, \tag{2.13}$$

which states that the azimuthal angle is uniformly distributed between 0 and 2π. The azimuthal angle after scattering is specified by a third random number, r_3, according to

$$\beta = 2\pi r_3. \tag{2.14}$$

If r_3 is uniformly distributed from zero to one, then β will be uniformly distributed from 0 to 2π.

The prescription for selecting the polar angle α is slightly more involved because S(k,$k^{'}$) may depend on α. By analogy with Eq. (2.12), we find

$$P(\alpha)d\alpha = \frac{\sin\alpha d\alpha \int_0^\infty \int_0^{2\pi} S(k,k^{'}) d\beta k^{'2} dk^{'}}{\int_0^{2\pi}\int_0^\infty \int_0^\pi [S(k,k^{'})\sin\alpha] d\beta k^{'2} dk^{'}}. \tag{2.15}$$

Consider an isotropic scattering mechanism like acoustic phonon scattering for which $S(k,k^{'}) = C_{AP}\delta(E^{'} - E)/\Omega$. Because C_{AP} is independent of α, Eq. 2.15 gives

$$P(\alpha)d\alpha = \frac{\sin\alpha d\alpha}{2}. \tag{2.16}$$

The angle, α, is specified by a fourth random number according to

$$P(r)dr = \frac{\sin\alpha d\alpha}{2}. \tag{2.17}$$

For a uniform random number generator, $P(r) = 1$, and

$$\int_0^{r_4} dr = \frac{1}{2}\int_0^{\infty} \sin\alpha d\alpha = \frac{1}{2}(1-\cos\alpha), \tag{2.18}$$

so that for isotropic scattering, α is determined by

$$\cos\alpha = 1 - r_4. \tag{2.19}$$

Note that β is uniformly distributed between 0 and 2π, but α is not uniformly distributed between 0 and π (rather, it is $\cos\alpha$ that is uniformly distributed between -1 and $+1$). For anisotropic scattering, small angle deflections are most probable. The procedure for selecting the polar angle begins with Eq. (2.15), but the appropriate $\mathrm{S}(k, k^{'})$ must be used.

2.2 MC simulation and the Boltzman Transport Equation

There has been considerable discussion in the literature about the connection between the Boltzmann transport equation and the ensemble Monte Carlo (EMC) technique. Most of this discussion relates to whether or not they yield the same results, and if so upon what time scale. In fact, it was easily pointed out many years ago that the MC procedure only approached the Boltzmann result in the long-time limit (Rees, 1969; Boardman *et al.*, 1970). Yet, there are still efforts to put more significance into the Boltzmann equation on the short time scale. The problem is that the Boltzmann equation is Markovian in its scattering integrals, a retarded, or non-Markovian, form of the Boltzmann equation is required for the short time scale. For this reason it needs to be mentioned that EMC technique supercedes the Boltzman transport equation even if it could be solved exactly in short time scales and therefore the EMC technique is intrinsically much more suited to tackle the high-field transport phenomena [10].

2.3 The evolution of the Bilkent EMC code

Initial steps in our group to develop an EMC code were taken in the spring of 2001 via the senior project of Mr. Engin Durgun, starting from Boardman's archaic code [11] (written in Fortran 66!) which was only a single-particle MC code. With the need for an *ensemble* MC (hence, EMC) approach, Tomizawa's code [7] in Fortran 77 was then adopted[2] which needed to be modernized, thanks to the modular programming tools provided by the f90 environment. Mr. Menderes Işkın's (fall 2001) and Mr. Serdar Özdemir's (spring 2002) senior projects made use of this code.

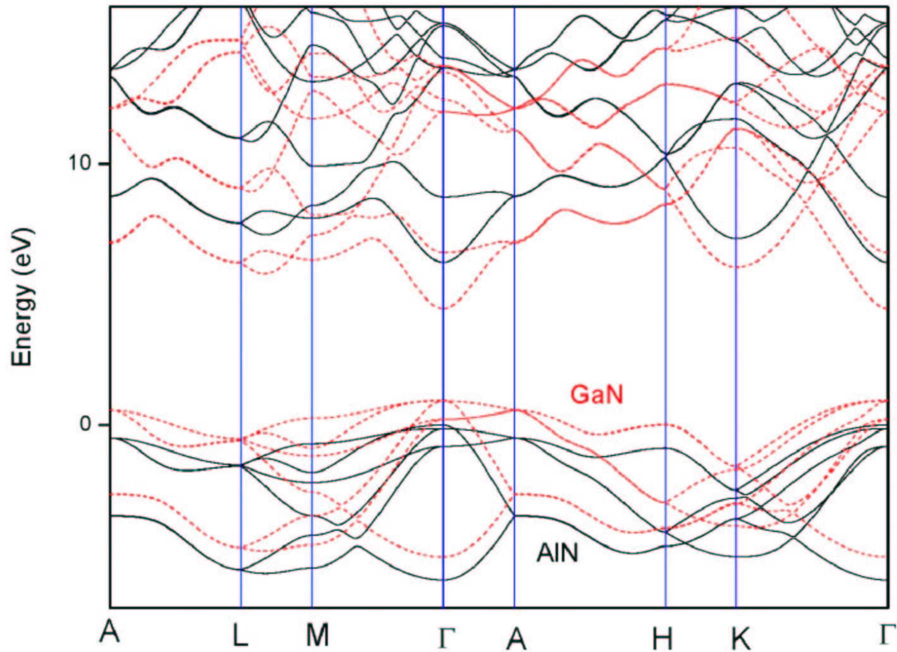

Figure 2.7: The empirical pseudopotential band structure of the GaN and AlN.

With the commencement of this thesis work in the summer of 2002, the simulation input parameters were separated into two parts, first one including the parameters that control the simulation and the other including the material properties. The code was split into a *motor* part and application-specific *drivers*,

[2]We gratefully acknowledge Prof. Tomizawa who kindly sent us this code.

such as bulk/APD/Gunn. The band structures were obtained using the empirical pseudopotential technique, see Fig. 2.7. The necessary band edge energy, effective mass and non-parabolicity parameters of all valleys in the lowest two conduction bands and valence bands located at high symmetry points were extracted through the computed bands of GaN and AlN; refer to Table A.1. All of major scattering mechanisms missing are added to EMC code which is controlled by switches in the simulation parameters input file. In particular, impact ionization and alloy scatterings have been given special emphasis; the details of our approach can be found in the Appendix.

The modified EMC code is used to simulate the both electrons and holes, within unipolar/bipolar diode structures. During the simulation, real density of states computed from the EPM band structure and the Lehmann-Taut procedure [9]. The simulation program is designed so that all of the output parameters can be recorded at each time step, which are then utilized to produce time-evolution movies via auxiliary codes in Matlab environment. Finally, a Python graphic user interface to Bilkent EMC code has been written by Dündar Yılmaz in the summer 2003. However, the construction work never ceases, some possible extensions are mentioned at the end of our final assessment in Chapter 6.

Chapter 3

Hot electron effects in *n*-type structures

GaN, AlN and their ternary alloys are becoming technologically important semiconductors, finding application in high power microelectronic devices such as GaN/AlGaN HEMTs as well as in optoelectronic devices like visible- and solar-blind AlGaN photodiodes[1]. The impact ionization (II) is an important process for all these devices subject to extreme electric fields. In the case of high power devices, II is undesired, leading to breakdown, whereas for devices like avalanche photodiodes, its sole operation relies on the II mechanism. The aim of this chapter is the analysis of II and related hot electron effects in GaN, AlN and their ternary alloys, all of which can support very high-field regimes, reaching few MV/cm values.

Surprisingly, there has been, as yet, no published measurement of the II coefficient for the $Al_xGa_{1-x}N$ system. To meet this demand from the computational side, very recently II in bulk AlGaN alloys has been analyzed [12], whereas in this work, we focus on device related aspects of II and hot electron effects. A useful model system for understanding hot electron effects is the unipolar $n^+ - n - n^+$ homojunction channel (cf. Fig. 3.1) which is to some extend impractical as it

[1] The contents of this chapter has been published in IEE Proceedings Optoelectronics [4].

gives rise to an excessive amount of current density. In the following sections we explain our computational procedure and present the transient and steady state hot electron phenomena taking place within this structure.

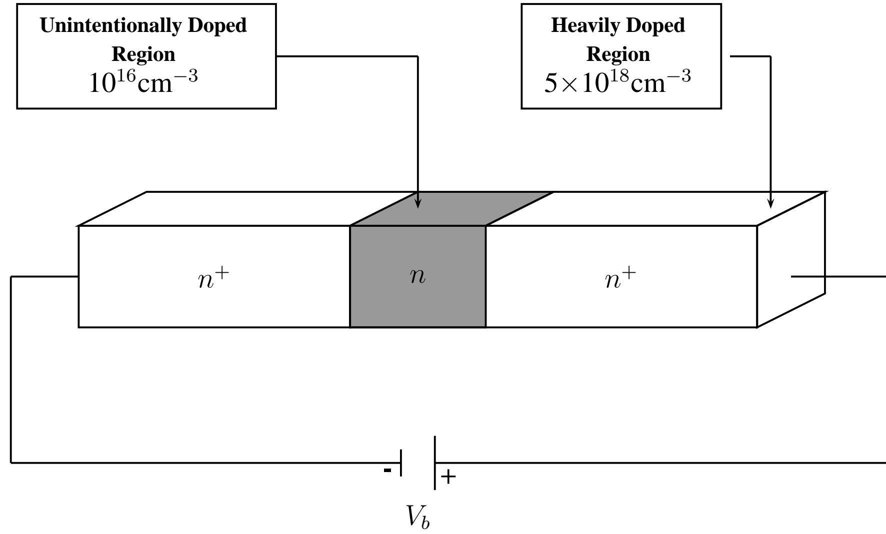

Figure 3.1: Structural schematic

3.1 Computational details

Our high-field transport methodology is based on the ensemble Monte Carlo technique [13], incorporating standard scattering processes: acoustic, non-polar and polar optical phonons, ionised impurity scattering, as well as alloy and II scatterings. We include all of the valleys in the lowest two conduction bands, aided by our empirical pseudopotential band structure calculations [14, 15]. We further append an additional higher-lying free electron band to account for the remaining bands. Due to emphasis of our work on II, the energy loss of the impacting electrons is accurately modeled [12]. We employ more than 20,000 electrons within the ensemble, for a total simulation time of about 7.5 ps. The time interval of invoking the Poisson solver is taken to be 0.1 fs.

3.2 Alloy scattering

The subject of alloy scattering has caused substantial controversy over the years which is still unsettled. In the case of group-III nitrides, Farahmand *et al.* [16] have dealt with this issue and reported that using the conduction band offset between the binary constituents as the alloy potential leads to an upper bound for alloy scattering. Being more conservative, for this value we prefer to use 0.91 eV, which is half of the corresponding GaN/AlN conduction band offset. Another source of concern has to do with the particular implementation of alloy scattering within the Monte Carlo simulation. Following Fischetti and Laux [17], we treat the alloy scattering as an intra-valley process with the distribution of the final scattering angles assumed to be isotropic, even though at higher energies it attains a forward directional character which should presumably weaken the effect of this mechanism on the momentum relaxation. Therefore, we are led to think that the effect of alloy scattering may still be overestimated.

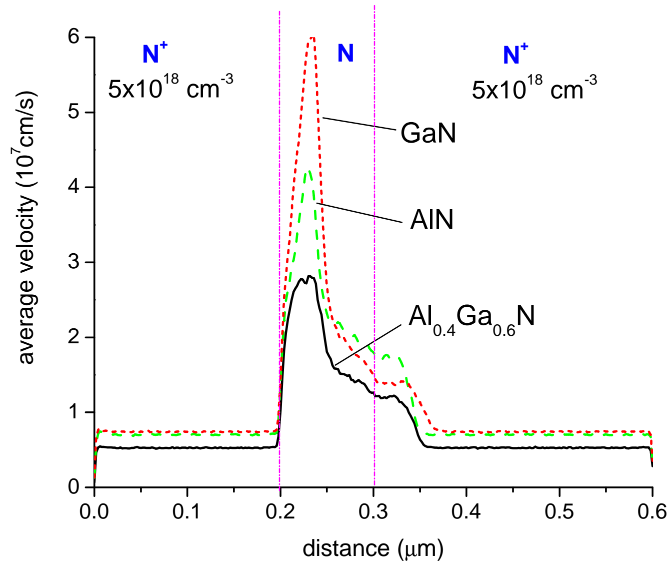

Figure 3.2: Velocity distribution over the $n^+ - n - n^+$ channel under an applied bias of 20 V.

3.3 Results

To gain insight into the high-field transport phenomena in GaN, AlN or $Al_xGa_{1-x}N$ based sub-micron sized dimensions we consider a simple $n^+ - n - n^+$ homojunction channel device [18] having 0.1 μm-thick unintentionally doped (10^{16} cm^{-3}) n region sandwiched between two heavily doped (5×10^{18} cm^{-3}) n^+ regions of thickness at least 0.2 μm thick; cf. Fig. 3.1. In Fig. 3.2 we show the velocity profiles for these materials; the $Al_{0.4}Ga_{0.6}N$ based structure suffers severely from alloy scattering and has a much reduced velocity. If we turn off the alloy scattering, then the curve for $Al_{0.4}Ga_{0.6}N$ (not shown) almost coincides with that of GaN. As a matter of fact, our previous analysis for bulk AlGaN alloys has identified the alloy scattering to modify the high energy electron distribution and lead to an increased II threshold [12].

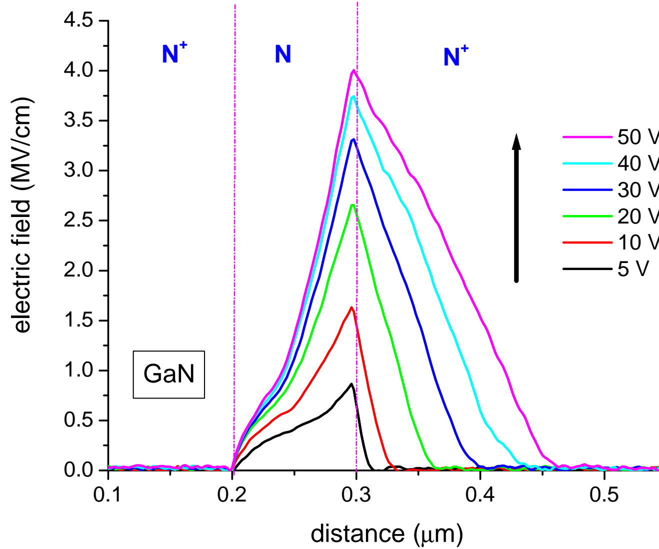

Figure 3.3: Electric field distribution over the $n^+ - n - n^+$ GaN channel at applied biases ranging from 5 V to 50 V.

The electric field along this device is distributed highly non-uniformly, reaching a few MV/cm values, which peaks at the right nn^+ interface, as shown in

Fig. 3.3 and Fig. 3.5 (a).

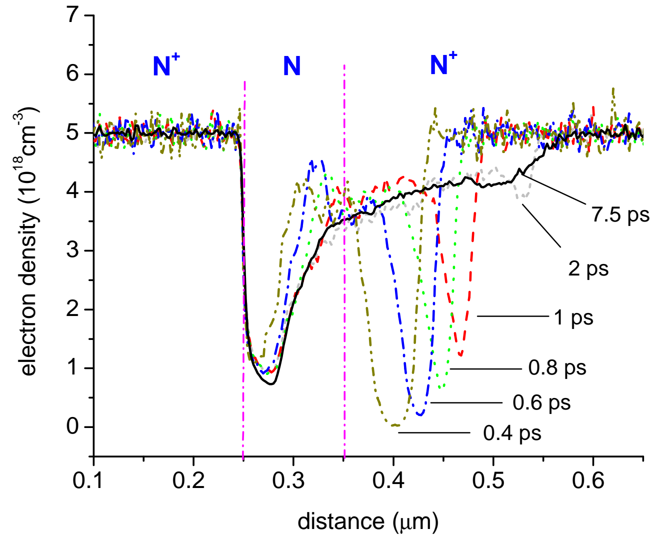

Figure 3.4: Time evolution of the transient electron density profile over the $n^+ - n - n^+$ GaN channel under an applied bias of 50 V; steady state result is also shown, evaluated at 7.5 ps.

Also note the penetration of the electric field into the heavily doped anode n^+ region with increasing applied bias, which amounts to widening of the unintentionally n-doped "base" region as in the Kirk effect; following Figures further support this viewpoint. The time evolution of the electron density profile is depicted in Fig. 3.4 starting from 0.4 ps. Oscillations around the unintentionally doped n region are clearly visible until steady state is established (7.5 ps curve in Fig. 3.4).

The fermionic degeneracy effects are seen to be operational at high fields and at high concentration spots. We make use of the Lugli-Ferry recipe [19] to account for degeneracy. However, if degeneracy is ignored, the electron distribution is observed to develop a dip in the n^+ anode region, shown in Fig. 3.5(a)

At a higher applied bias (80 V in GaN) the effect of II becomes dominant. As illustrated in Fig. 3.5 (b), this mechanism introduces a substantial energy loss

mechanism for the energetic carriers that have just traversed the unintentionally doped n region.

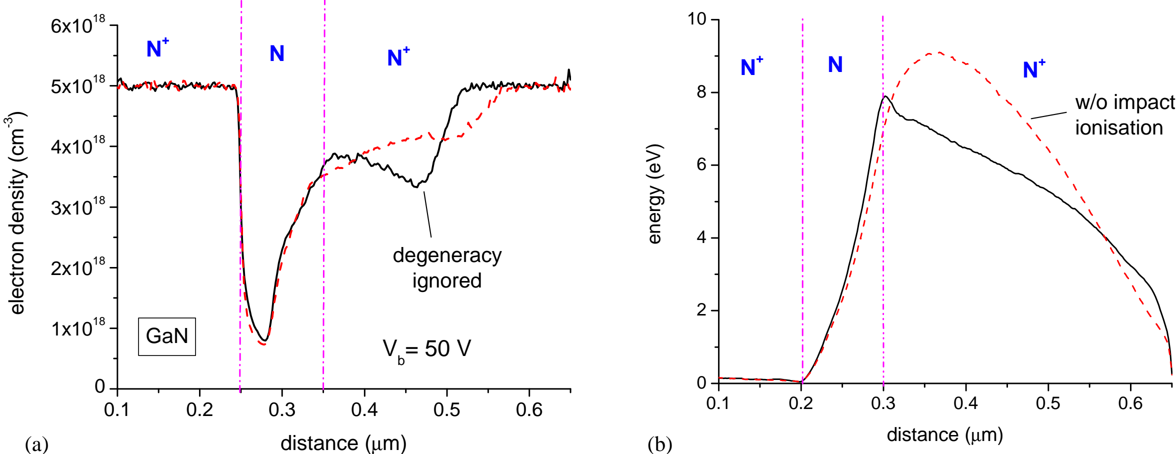

Figure 3.5: (a) Steady state density profile at a bias of 50 V, with and without the degeneracy effects included. (b) Energy distribution over the $n^+ - n - n^+$ GaN channel under an applied bias of 80 V, with and without impact ionization being included.

Chapter 4

AlGaN solar-blind avalanche photodiodes

Achieving ultraviolet solid-state photodiodes having internal gain due to avalanche multiplication is a major objective with a potential to replace photomultiplier tube based systems for low-background applications[1] [20]. The $Al_xGa_{1-x}N$ material with the Aluminium mole fraction, $x \geq 0.38$ becomes a natural candidate for the solar-blind avalanche photodiode (APD) applications which can also meet high-temperature and high-power requirements. Unfortunately, due to growth-related problems, such as high defect and dislocation densities causing premature microplasma breakdown, there has been as yet no experimental demonstration of an APD with the $Al_xGa_{1-x}N$ material. As a matter of fact, even for the relatively mature GaN-based technology, few reports of observation of avalanche gain exist [21, 22, 23, 24].

While the material quality is being gradually improved, our aim in this chapter is to meet the immediate demand to explore the prospects of (Al)GaN based APDs from a computational perspective. Within the last decade, several techniques have been reported which model gain and time response of APDs. Most,

[1] The contents of this chapter has been recently published in Applied Physics Letters [5].

however, approximate the carriers as always being at their saturated drift velocity and impact ionization rates are usually assumed to depend only on the local electric field; for references, see Ref. [25]. While nonlocal effects have recently been incorporated [26], the dubious assumption on carrier drift velocity remains. Among all possible techniques, the ensemble Monte Carlo (EMC) method is potentially the most powerful as it provides a full description of the particle dynamics. However, only a small number of such simulations have been reported, predominantly on GaAs based APDs [27, 28].

4.1 Computational details

As mentioned several times before, for the high-field transport phenomena, the EMC technique is currently the most reliable choice, free from major simplifications [29]. All standard scattering mechanisms are included in our EMC treatment other than dislocation, neutral impurity and the piezoacoustic scatterings as they only become significant at low temperatures and fields [30]. Impact ionization parameters for bulk GaN are extracted from a recent experiment of Kunihiro *et al.* [31]. As for the case of AlN, due to lack of any published results, we had to resort to a Keldysh approach, while Bloch overlaps were taken into account via the f-sum rule [10]; for details, see Ref. [12]. Furthermore, the polar optical phonon and ionized impurity potentials are screened by using random phase approximation based dielectric function [32].

The band structures for GaN and AlN are obtained using the empirical pseudopotential technique fitted to available experimental results and first principles computations [14, 15]. For the alloy, $Al_xGa_{1-x}N$, we resort to linear interpolation (Vegard's Law) between the pseudopotential form factors of the constituent binaries. The necessary band edge energy, effective mass and non-parabolicity parameters of all valleys in the lowest two conduction bands and valence bands located at high symmetry points are extracted through the computed bands of GaN and $Al_xGa_{1-x}N$. To account for the remaining excited conduction and valence bands, we further append additional higher-lying parabolic free electron and

hole bands. At this point it is important to stress that we use the actual density of states computed using the Lehmann-Taut approach [9], rather than the valley-based non-parabolic band approximation, in calculating the scattering rates [33]. This assures perfect agreement with rigorous full-band EMC simulations [34] even for the hole drift velocities at a field of 1 MV/cm.

During the computation the Schottky barrier height is neglected in comparison to the applied very high reverse bias, whereas, it needs to be included in the case of a forward bias. Similarly, this eliminates the subtle complications regarding the choice of a suitable boundary condition, hence, we use the standard neutral-contact model which keeps the charge density constant at the boundary regions via injecting or removing majority/minority carriers. To decrease the statistical noise on the current, we employ more than 60,000 superparticles within the ensemble, and use the higher-order triangular-shaped-cloud representation of the superparticle charge densities [35]. The Poisson solver is invoked in 0.25 fs time intervals not to cause an artificial plasma oscillation. All computations are done for a temperature of 300 K. To avoid prolonged transients following the sudden application of a high-field, the reverse DC bias is gradually applied across the APD over a linear ramp within the first 1.25 ps.

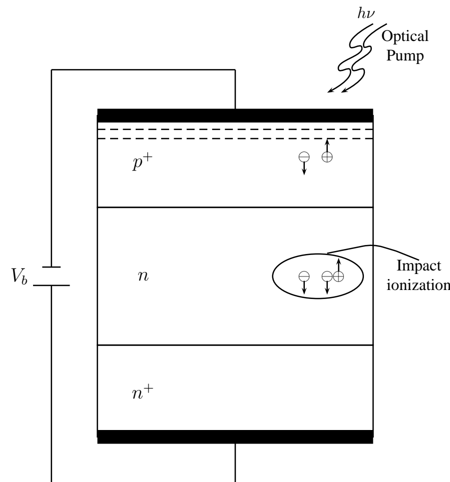

Figure 4.1: Structural details.

4.2 Results

In the following subsections, we only deal with the gain and temporal response of the GAN and AlGaN APDs. Other important properties, such as noise and spectral response are not included in this work.

4.2.1 GaN APDs

Even though, our principal aim is to characterize solar-blind APDs attainable with the band gap of $Al_{0.4}Ga_{0.6}N$, we first test the performance of our methodology on GaN-based visible-blind APDs where a few experimental results have recently been reported [21, 22, 23, 24]. Among these, we choose the structure (Fig. 4.1) reported by Carrano *et al.* [23] having 0.1 μm thick unintentionally doped (10^{16} cm^{-3}) n (multiplication) region sandwiched between 0.2 μm thick heavily doped (10^{18} cm^{-3}) p^+ region and a heavily doped (10^{19} cm^{-3}) n^+ region. Fig. 4.2(a) shows that the current gain of this structure where, following Carrano

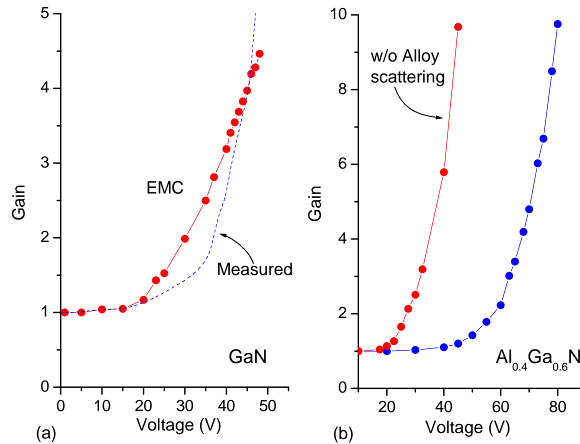

Figure 4.2: (a) Current gain of the GaN APD; EMC simulation (symbols) compared with measurements [23] (dotted). (b) Current gain of the $Al_{0.4}Ga_{0.6}N$ APD simulated using EMC with and without alloy scattering. Full lines in EMC curves are used to guide the eye.

et al., the current value at 1 V is chosen as the unity gain reference point. The overall agreement between EMC and the measurements [23] is reasonable. Notably, EMC simulation yields somewhat higher values over the gain region, and the breakdown at 51 V cannot be observed with the simulations. Nevertheless, given the fact that there is no fitting parameter used in our simulation, we find this agreement quite satisfactory.

An important characteristic of the APDs is their time response under an optical pulse. For this purpose, an optical pump is turned on at 6.25 ps creating electron-hole pairs at random positions consistent with the absorption profile of the electromagnetic radiation with a skin depth value of 10^{-5} cm for GaN. The photon flux is assumed to be such that an electron-hole pair is created in 0.5 fs time intervals. The optical pump is kept on for 25 ps to assure that steady state is attained and afterwards it is turned off at 31.25 ps to observe the fall of the current. As we are assuming a p-side illumination, it is mainly the *electrons* which travel through the multiplication region, even though in the simulation the impact ionization of both electrons and holes are included.

The falling edge of the optical pulse response can be fitted with a Gaussian profile $\exp(-t^2/\tau_f^2)$, see parameters in Table 4.1. As seen in Fig. 4.3 and Table 4.1,

Table 4.1: Fitted temporal response functions $\exp(-t^2/\tau_f^2)$ and $1 - \exp(-t^2/\tau_r^2)\cos(\omega_r t)$ for the GaN APD.

Bias (V)	τ_f (ps)	τ_r (ps)	ω_r (r/ps)
25	1.72	3.06	0.35
30	1.78	2.57	0.38
40	2.04	1.75	0.506

the width of the Gaussian profile increases with the applied bias. Hence, the temporal response of the device degrades in the high gain region where substantial amount of secondary carriers exist, as expected. The rising edge of the pulse shows an underdamped behavior, becoming even more pronounced towards the gain region; this can *approximately* be fitted by a function $1 - \exp(-t^2/\tau_r^2)\cos(\omega_r t)$, with the parameters being listed in Table 4.1.

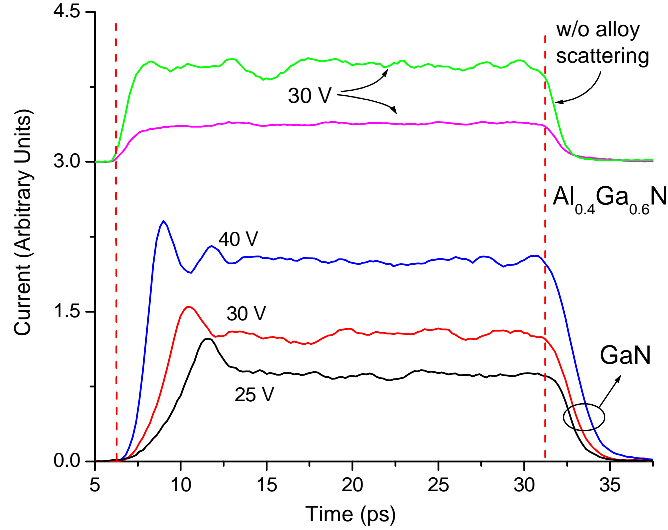

Figure 4.3: Temporal response of the GaN and $Al_{0.4}Ga_{0.6}N$ (vertically shifted for clarity) APD to a 25 ps optical pulse, applied between the dashed lines.

Fig. 4.4(a) demonstrates the electric field profile of the GaN APD. Observe that as the applied bias increases the moderately doped p^+ region becomes vulnerable to the penetration of the electric field, hence preventing further building up in the multiplication region and increasing the impact ionization events. In this regard, it needs to be mentioned that achieving very high p doping persists as a major technological challenge. Therefore, in our considerations to follow for the AlGaN APDs, we replace the problematic p^+ region with a Schottky contact.

4.2.2 Schottky contact-AlGaN APDs

With this insight, we analyze an $Al_{0.4}Ga_{0.6}N$ APD of 0.1 μm thick unintentionally doped (10^{16} cm^{-3}) n region sandwiched between a Schottky contact and a heavily doped (10^{19} cm^{-3}) n^+ region.

Previously, in unipolar AlGaN structures we observed the alloy scattering to be substantial (Chapter 3)[4], whereas the actual significance of this mechanism

has always been controversial [10]. For this reason, we provide in Fig. 4.2(b) the gain characteristics of this $Al_{0.4}Ga_{0.6}N$ APD both with and without alloy scattering. The presence of alloy scattering almost doubles the breakdown voltage with respect to the case when there is no alloy scattering.

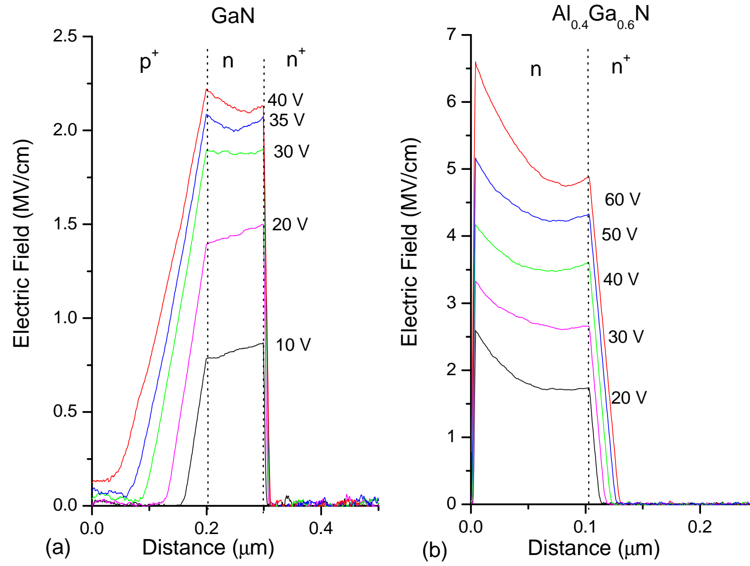

Figure 4.4: Electric field distribution over (a) GaN (b) $Al_{0.4}Ga_{0.6}N$ APDs at several bias levels.

The time response of the $Al_{0.4}Ga_{0.6}N$ APD is shown in Fig. 4.3 in the low gain region (30 V) under the same optical illuminations discussed in the GaN case, above. The falling edge of the response can be fitted by an exponential $\exp(-t/\tau_f)$ whereas the rising edge by a Gaussian function, $1-\exp(-t^2/\tau_r^2)$; see Table 4.2 for the parameters.

Fig. 4.4(b) demonstrates the electric field profile of this $Al_{0.4}Ga_{0.6}N$ structure. It is observed that for all values of the applied bias, the electric field is confined in the intrinsic (multiplication) region which is very desirable for the APD operation. Finally, we would like to check the standard assumption made in other theoretical APD treatments assuming the carriers to travel at their saturated drift velocities.

Table 4.2: Fitted temporal response functions $\exp(-t/\tau_f)$ and $1 - \exp(-t^2/\tau_r^2)$ for $Al_{0.4}Ga_{0.6}N$ APD under a reverse bias of 30 V.

Alloy Scattering	τ_f (ps)	τ_r (ps)
No	0.75	0.67
Yes	1.06	2.14

It is seen in Fig. 4.5 that this assumption may be acceptable for the Schottky structure having a uniform field distribution within the multiplication region, whereas it is not appropriate in the $p^+ - n - n^+$ case with our doping values. Also it should be noted that, some of the wild oscillations in the n-region of Fig. 4.5(a) are possibly due to poor statistical averaging of our EMC simulation[2].

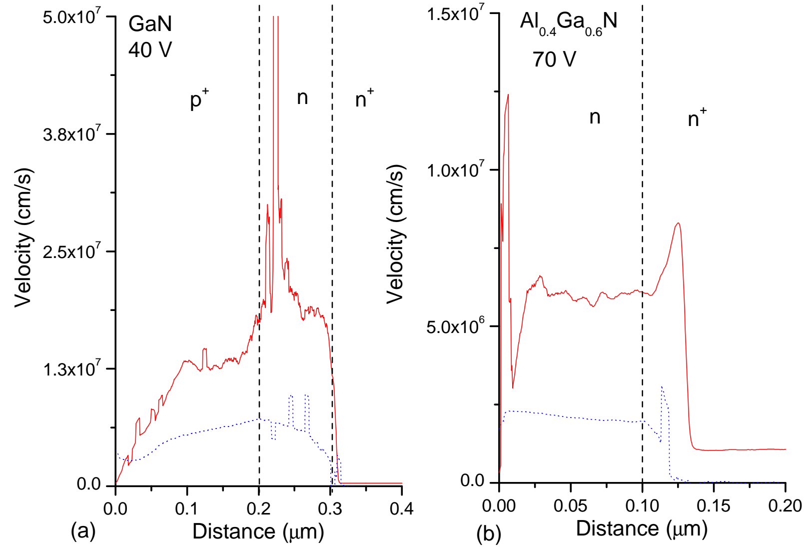

Figure 4.5: Average velocity distribution over (a) GaN (b) $Al_{0.4}Ga_{0.6}N$ APDs for electron (solid) and holes (dotted).

[2]This point has been kindly brought to our attention by Prof. Cengiz Beşikçi.

Any experimental support, which is currently impeded by the poor AlGaN material quality, will be extremely valuable to further refine our models. In other words, our simulations await to be verified or falsified by other researchers.

Chapter 5

Gunn oscillations in GaN channels

At high electric fields, the electron velocity, v, in GaAs, GaN, AlN, and some other compound semiconductors decreases with an increase in the electric field, F, so that the *differential mobility*, $\mu_d = dv/dF$ becomes negative (see Fig. 5.1). Ridley and Watkins in 1961 and Hilsum in 1962 were first to suggest that such a *negative differential mobility* in high electric fields is related to an electron transfer between different valleys of the conduction band (*intervalley transfer*). When the electric field is low, electrons are primarily located in the central valley of the conduction band. As the electric field increases many electrons gain enough energy for the *intervalley transition* into higher satellite valleys. The electron effective mass in the satellite valleys is much greater than in the central valley. Also, the intervalley transition is accompanied by an increased electron scattering. These factors result in a decrease of the electron velocity in high electric fields. There are other mechanisms than the intervalley transfer to achieve negative differential mobility as well [36]. From the technological point of view, this effect is exploited to build oscillators up to Terahertz frequencies.

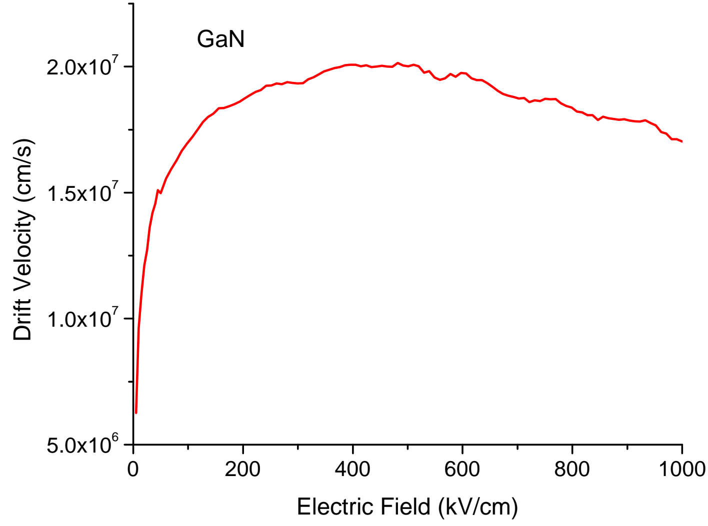

Figure 5.1: EMC simulation of the drift velocity versus field for bulk GaN at 300 K.

5.1 Basics

A simplified equivalent circuit [37] of a uniformly doped semiconductor may be presented as a parallel combination of the differential resistance (see Fig. 5.2)

$$R_d = \frac{L}{q\mu_d n_0 S}, \tag{5.1}$$

and the differential capacitance:

$$C_d = \frac{\varepsilon S}{L}. \tag{5.2}$$

Here S is the cross section of the sample, L is the sample length, and n_0 is the electron concentration.

The equivalent RC time constant determining the evolution of the space charge is given by

$$\tau_{md} = R_d C_d = \frac{\varepsilon}{q\mu_d n_0}, \tag{5.3}$$

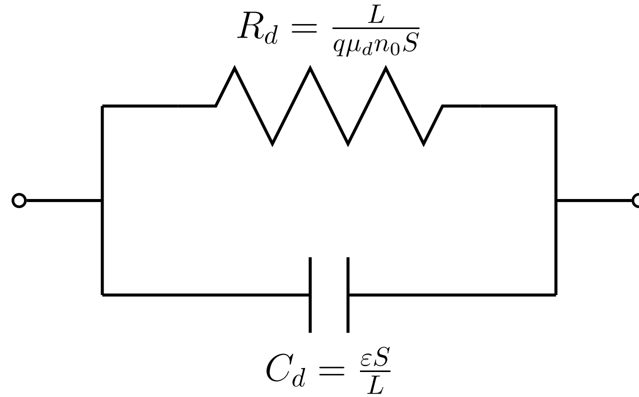

Figure 5.2: Equivalent circuit for a uniform piece of semiconductor.

where, τ_{md} is called the differential dielectric relaxation time or Maxwell dielectric relaxation time. In a material with a positive differential conductivity, a space charge fluctuation decays exponentially with this time constant. However, if the differential conductivity is negative, the space charge fluctuation may grow with time. What actually happens depends on the relationship between τ_{md} and the electron transit time, $\tau_{tr} = L/v$. If (-τ_{md}) $\gg \tau_{tr}$, a fluctuation of the electron concentration occurring near the negatively biased terminal (cathode) grows very little during its transit time toward the positively biased terminal (anode). However, when (-τ_{md}) $\ll \tau_{tr}$, a space charge fluctuation grows tremendously during a small fraction of the transit time. In this case, it develops into a high-field region (called a *high-field domain*), which propagates from the cathode toward the anode with the velocity that is approximately equal to the electron saturation velocity, v_s.

The condition (-τ_{md}) $\ll \tau_{tr}$ leads the following criterion of a high-field domain formation:

$$n_0 L \gg \frac{\varepsilon v_s}{q|\mu_d|}. \tag{5.4}$$

For $v = 10^5$ m/s, $|\mu_d| \simeq 0.15$ m^2/Vs, $\varepsilon = 1.14\times10^{-10}$ F/m, we obtain $n_0 L \gg 1.5\times10^{11}$ cm^{-2}. This condition (first introduced by Professor Herbert Krömer in 1965) is called the Krömer criterion. On the experimental side, Ian Gunn

was first to observe high-field domains in GaAs in 1963. Ever since, these GaAs two-terminal devices are often called Gunn diodes

5.2 Motivation

The negative differential mobility threshold field due to intervalley carrier transfer for GaN is quite high, above 200 kV/cm, which becomes appealing for building very high power millimeter-wave oscillators (see Fig. 5.1). In addition to their technological importance, these Gunn diodes still pose a number of physical puzzles, such as the detailed understanding of the domain nucleation process in different doping profiles [38]. Also, the onset of chaotic behavior [39] in these structures is another intriguing subject. As a matter of fact, the presence of impact ionization has been reported to give rise to chaotic multi-domain formation [40]. This result was based on a numerical solution of a set of partial differential equations under simplifying assumptions. The ensemble Monte Carlo (EMC) approach is believed to be much better suited for this task [41], and, for instance, it has been successfully tested in the analysis of InP Gunn diodes [42].

An ever-present objective is to increase the operating frequency of the Gunn diodes. This can be achieved in several ways. Our approach is to operate the Gunn diodes at their higher harmonic frequencies rather than the fundamental. However, the drawback here is the very low efficiency associated with these high harmonic modes. Therefore, we devote much of this chapter to the harmonic RF conversion efficiency enhancement by all means.

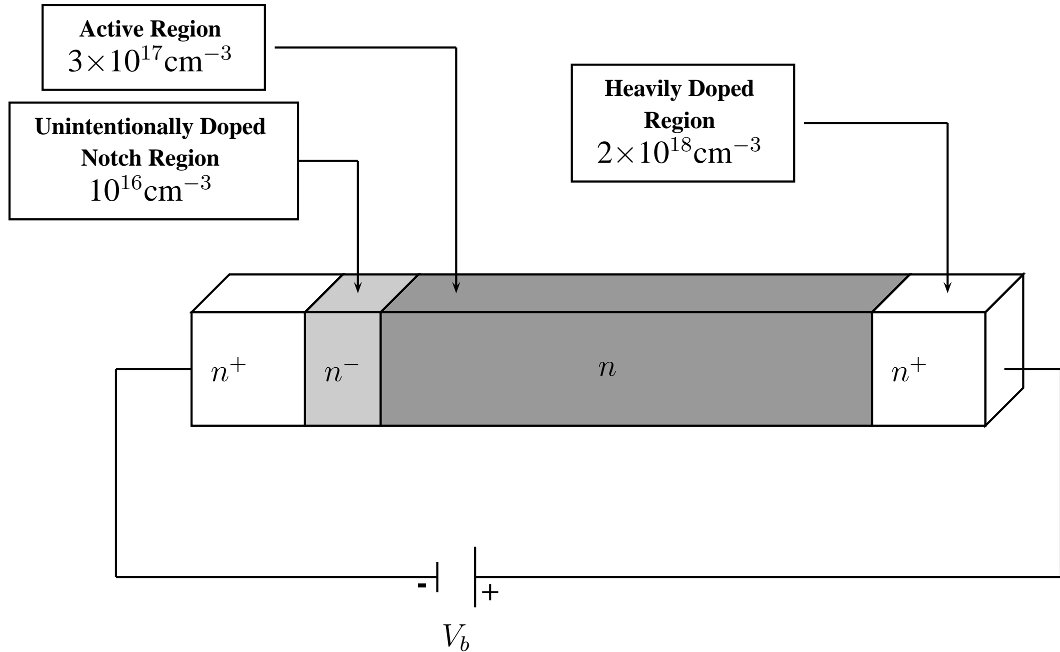

Figure 5.3: Structural details.

5.3 Computational details

Along this line, here we employ the EMC method to shed light on the dynamics of millimeter-wave Gunn domain oscillations with large amplitudes in GaN channels. The same GaN material was the subject of another recent study with an emphasis on multiple-transit region effects on the output power [43]. Unfortunately, their analysis utilized unrealistic values for the two important satellite valleys, chosen as 2.27 eV and 2.4 eV above the conduction band edge. These are about 1 eV higher than the experimental and theoretical values. In this work, as mentioned before, the necessary band structure data is extracted from our empirical pseudopotential calculations [14] fitted to available experimental and theoretical data. An analytical-band variant of EMC is preferred that enables a vast number of simulations. Very good agreement of such an approach with full band EMC results [44] gives further confidence for this choice. Moreover, we use the actual density of states, rather than the valley-based non-parabolic bands in

forming the scattering tables [45].

The basic structure we investigate is of the form, $n^+ - n^- - n - n^+$, with the active region being formed by the n^- notch with a doping of 10^{16} cm^{-3} and the main n-doped channel having 3×10^{17} cm^{-3} doping; the n^+ contact regions are assumed to have 2×10^{18} cm^{-3} dopings; see, Fig 5.3. The length of the notch region is varied to investigate its effect on the harmonic operation, while keeping the total length of the active region ($n^- - n$) constant at 1.2 μm. Our EMC simulations all start from a neutral charge distribution, and unless otherwise stated, are at 300 K. As a standard practice in modeling Gunn diodes (see, Ref. [38] and references therein), a single-tone sinusoidal potential of the form $V_{DC}+V_{AC}\sin(2\pi ft)$ is imposed across the structure; in our work V_{DC}=60 V and V_{AC}=15 V (if not stated). This choice significantly simplifies our frequency performance analysis; its validity will be checked later on. The oscillator efficiency is defined as $\eta = P_{AC}/P_{DC}$, where P_{AC} is the time-average *generated* AC power and P_{DC} is the *dissipated* DC power by the Gunn diode. Therefore, a negative efficiency corresponds to a resistive (dissipative) device and a positive value designates an RF conversion from DC.

5.4 Results

Fig. 5.4(a) displays Gunn domains for operations at the fundamental, second, third and fourth harmonic frequencies for a 250 nm notch device[1]. As usual, the domains build up as they approach to the anode side. Fig. 5.4(b) illustrates the evolution of the electric field in one period for the fundamental frequency operation (122.5 GHz). It can be noted that due to the relatively wide notch width, significant amount of the electric field accumulates around this region, with a value that can exceed 1.2 MV/cm (under a DC bias of 60 V), reaching impact ionization threshold [12]. To analyze this further, we increased the DC bias to 90 V and the operating temperature to 500 K; the effect of turning off the impact ionization mechanism was observed to be marginal even at these extreme

[1] A part of this section will be published in Semiconductor Science and Technology.

conditions for all notch widths considered.

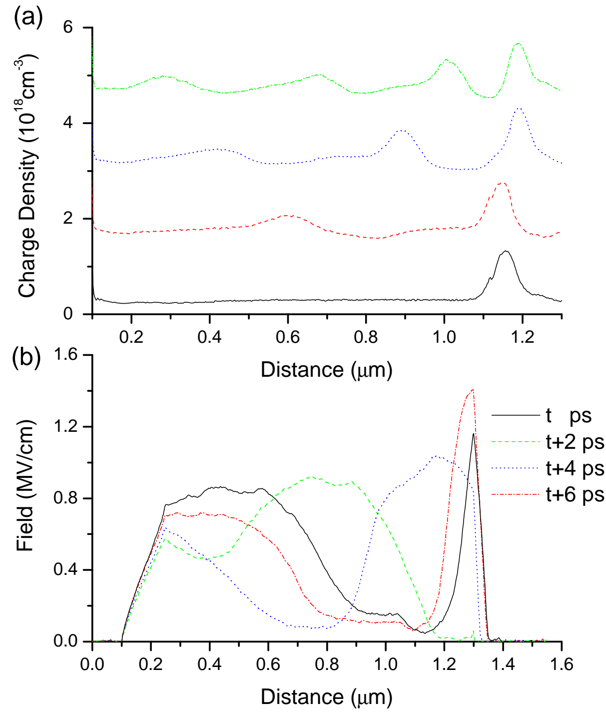

Figure 5.4: (a) Typical charge density profiles for a 250 nm-notch device operating at the fundamental, second, third, fourth-harmonic modes, each respectively vertically up-shifted for clarity. (b) Time evolution of the electric field profile within one period of the Gunn oscillation at 2 ps intervals for the 250 nm-notch device.

5.4.1 The effect of notch width

In Fig. 5.5(a) different notch widths are compared in terms of their frequency performance. Our main finding is that, by increasing the notch width, GaN Gunn diodes can be operated with more efficiency at their second harmonic frequency than the fundamental, as seen for the 250 nm notch-width curve. However, we observed that further increasing the notch width above 400 nm gives rise to total loss of the Gunn oscillations. These results are extracted from long simulations

up to 500 ps to capture the steady state characteristics at each frequency, which becomes quite demanding. Hence, the Pauli degeneracy effects requiring extensive memory storage are not included. Fig. 5.5(b) illustrates the effect of including the Pauli exclusion principle using the Lugli-Ferry recipe [19, 4]. Note that for Gunn diodes, this effect is quite negligible, slightly lowering the resonance frequencies at higher harmonics.

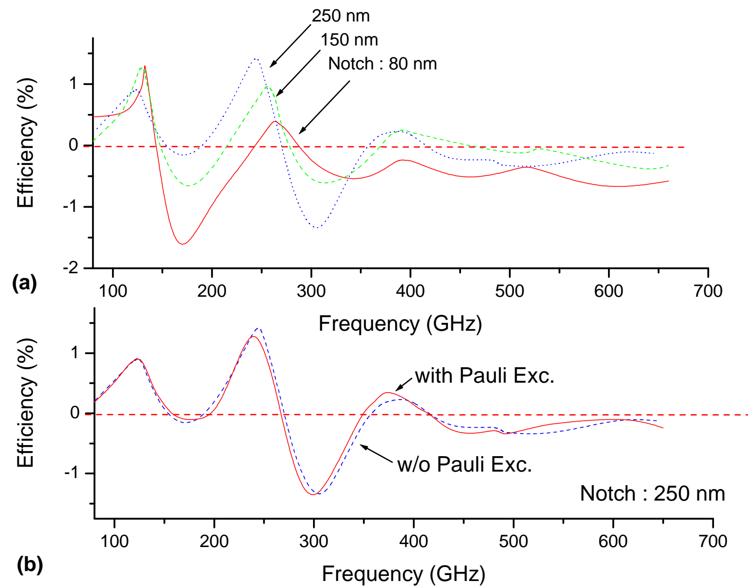

Figure 5.5: Gunn diode efficiency versus frequency. (a) Effect of different doping-notch widths, while keeping the total active channel length fixed at 1.2 μm. (b) Effect of including the Pauli exclusion principle for the 250 nm-notch device.

5.4.2 The effect of lattice temperature

Being a unipolar device, Gunn diodes operate under high current levels which leads to excessive heating of the lattice. Therefore, we would like to consider the effects of temperature on our results, picking 250 nm-notch device (being the most promising one in harmonic enhancement). As seen in Fig. 5.6, in response to an increase in the lattice temperature, second harmonic efficiency increases where as the fundamental and third harmonic efficiencies decrease. Also, as expected the curves shift to lower frequencies due to increased phonon scattering which reduces the carrier saturation velocity and hence the Gunn oscillation frequency. The important finding is that at even higher lattice temperatures the second-harmonic efficiency is further reinforced.

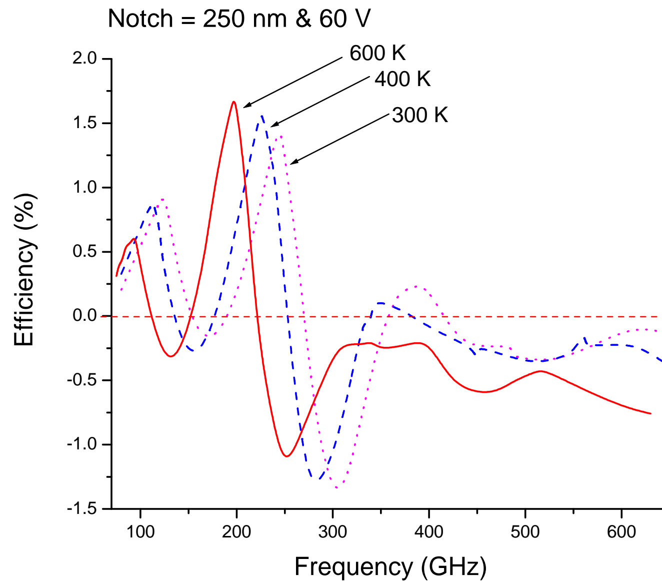

Figure 5.6: RF conversion efficiency versus frequency for several lattice temperatures; 250 nm-notch device at 60 V bias is used.

5.4.3 The effect of channel doping

Next, we consider the effect of the channel doping again using the same 250 nm-notch device for comparison purposes. One can easily observe from Fig. 5.7 that the channel doping is highly critical in the operation of the Gunn diodes. This doping is mainly instrumental in the differential dielectric relaxation time (see Eq. 5.3) which decreases as the doping increases. For relatively low channel dopings, the $-\tau_{md} \ll \tau_{tr}$ condition gets violated which explains the behavior displayed in Fig. 5.7. Furthermore, at lower channel dopings, not only the AC current magnitude is decreased but also the phase angle difference with respect to AC voltage shifts from active toward lossless and dissipative regimes. If the channel doping is increased beyond 3×10^{17} cm^{-3} than the part of the active channel on the anode side begins to act like a contact, reducing the dimension of the active channel length, hence increasing the Gunn oscillation frequency.

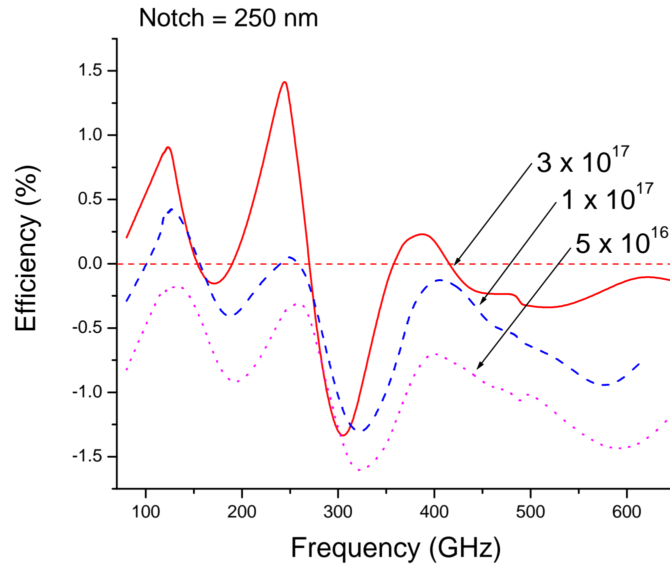

Figure 5.7: RF conversion efficiency versus frequency for several channel dopings; 250 nm-notch device at 60 V bias is used.

5.4.4 The effect of DC operating point

Another parameter that can affect the achievement of harmonic enhancement is the DC operating point. Not to lose the grounds for comparison, we need to scale the RF amplitude while changing the applied DC voltage across the Gunn diode. Hence, we simulate the same 250 nm-notch Gunn diodes operating under three different DC and RF bias levels which are 50 V DC bias with 12.5 V RF bias, 60 V DC bias with 15 V RF bias, 70 V DC bias with 17.5 V RF bias. The important observation is that the harmonic enhancement is favored towards the critical field at which negative differential mobility sets in (50 V case in Fig. 5.8).

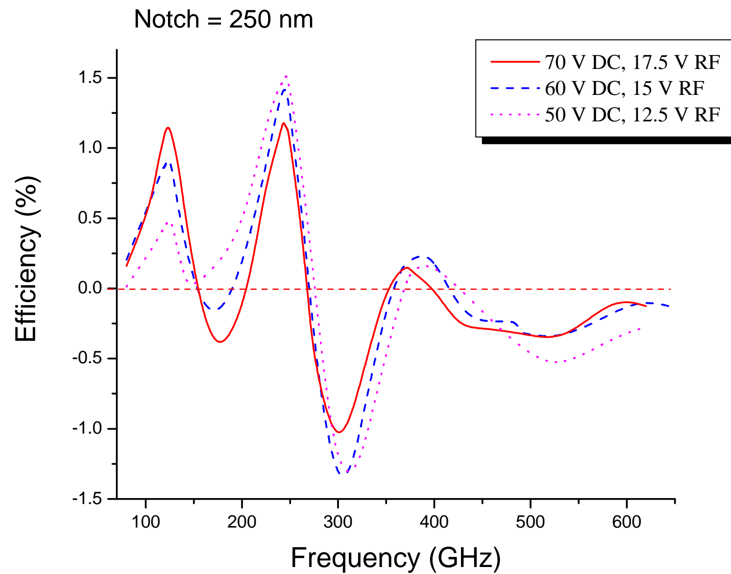

Figure 5.8: RF conversion efficiency versus frequency for several DC bias voltages; 250 nm-notch device.

5.4.5 Connecting to a tank circuit

Finally, we relax the imposed single-tone sinusoidal voltage across the Gunn diode and connect it to an external tank circuit with the voltage across the device being self-consistently updated at each simulation step (0.4 fs) through solving in time-domain a Gunn diode in parallel with a capacitor and a resistor, all in series with an inductor and a DC source (cf. Fig. 5.9(b) inset). The AC voltage and current of the Gunn diode are shown in Figs. 5.9(a) and (b), comparing respectively the imposed single-tone bias with the tank circuit tuned to the fundamental frequency of the 150 nm notch device. For both cases the current and voltage are in anti-phase with each other leading to RF generation as intended; the main discrepancy being higher harmonic content in the tank circuit case as governed by the quality factor of the resonator.

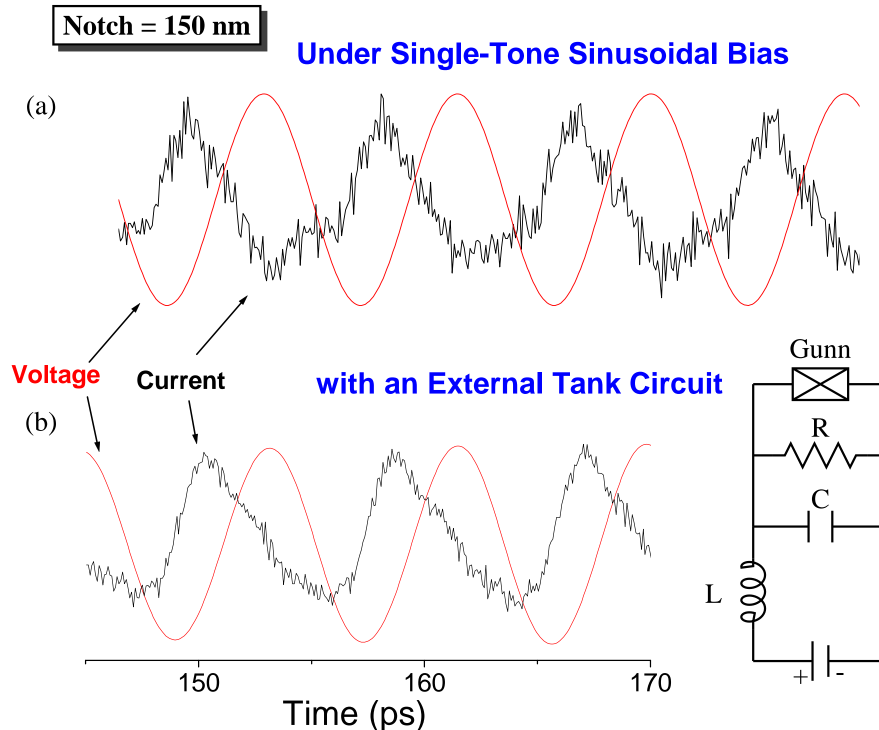

Figure 5.9: Current and voltage waveforms for a 150 nm-notch Gunn diode (a) under an imposed single-tone sinusoidal voltage, and (b) connected to an external tank circuit shown in the inset.

5.5 Computational budget

Finally, we would like to give some details about the computational load of our simulations. All of our computations have been carried on a dedicated Pentium-4 3.06 GHz PC running on a Linux (RedHat v8.0) operating system, complied with the most recent Intel 7.1 Fortran complier. To give some idea, the Gunn simulations of this chapter have been completed in about 3.5 months non-stop. The memory requirement of a typical run is less than 5 Mb which increases to 1.1 Gb when Pauli exclusion principle as implemented by the Lugli-Ferry recipe is included as in Fig. 5.5(b).

Chapter 6

Summary of the main findings

This work has been devoted to the investigation of the high field transport phenomena in wide bandgap semiconductors such as (GaN, AlGaN and AlN). With this objective, an EMC-based simulation tool has been developed. All of major scattering mechanisms have been added, capable of simulating both electrons and holes, within unipolar/bipolar diode structures.

First, we considered GaN, AlGaN and AlN based unipolar homojunction channel devices to gain insight to the high-field transport phenomena. We examined the velocity, electric field profiles and time evolution of the electron density in these materials. Our first finding was that the $Al_{0.4}Ga_{0.6}N$-based structures suffer severely from alloy scattering and possess a much reduced drift velocity. When we turned off the alloy scattering, the curve for $Al_{0.4}Ga_{0.6}N$ has almost coincided with that for GaN. The electric field profile along this device was distributed highly non-uniformly, reaching a values of few MV/cm, peaking at nn^+ interface and also penetrating into the heavily doped anode n^+-region as the applied bias is increased. In time evolution of the electron density oscillation around the unintentionally doped n-region were observed until steady state is established. Fermionic degeneracy effects were seen to be operational at high fields and high concentration spots. At very high fields II was shown to introduce a substantial energy loss mechanisms for the energetic carriers that have just traversed the unintentionally doped n-region.

Next, we analyzed multiplication and temporal response characteristic of GaN and Schottky $Al_{0.4}Ga_{0.6}N$ APDs. To check our model, we simulated the structure reported by Carrano *et al.* [23] and obtained reasonable agreement. Examining the time response of APDs under a pico-second optical illumination, an underdamped step response was observed in the rising edge and a Gaussian profile damping in the falling edge. For the electric profile of the GaN APD, we noted that as the applied bias increases the electric field increases along the p^+ region. To increase the electric field at the multiplication region, we replaced the problematic p^+-region with a Schottky contact and simulated the Schottky-contact $Al_{0.4}Ga_{0.6}N$ APD. As intended, for all values of the applied bias, the electric field was observed to be confined in the multiplication region. For the gain characteristics of Schottky contact $Al_{0.4}Ga_{0.6}N$ APD both with and without alloy scattering and we found that the presence of alloy scattering doubles the breakdown voltage.

Finally, we studied the Gunn domain oscillations under both impressed single-tone sinusoidal bias and external tank circuit conditions. In particular, our motivation was to seek all means to enhance the harmonic RF conversion in comparison to the fundamental mode operation. Hence, we examined the effect of the notch width on the higher harmonic frequencies and found that GaN Gunn diodes can be operated with more efficiency at their second harmonic frequency for wide-enough notch regions. However, there exists an upper limit the width of this region beyond which Gunn oscillations ceases altogether. Moreover, the Pauli degeneracy effect and impact ionization scattering were seen to be quite negligible. Furthermore, increasing the lattice temperature or the channel doping was observed to enhance the second harmonic efficiency. Finally, we studied the Gunn diodes operating under different DC bias levels; the fundamental mode was seen to be affected by far, compared to higher harmonics.

At this point, we would like to mention some possible extension of this work. Being a close relative of the devices considered here, IMPATT diodes can also be studied using the some infrastructure. On the more basic research side, it is intriguing to explore chaos in Gunn diodes [53], and other high field devices. From a technical perspective, other scattering mechanisms can be included such as the carrier-carrier scattering, and for low temperature and poor quality samples the

dislocation scattering. Finally, the code can be upgraded to a fullband EMC [54] and even employing ab-initio bandstructure techniques rather than the EPM. However, our current analytical-band EMC tool will still preserve its place, as it is still the preferred choice for extensive simulations to test certain *ideas*, as we have done in pursing the harmonic enhancement in Gunn diodes.

Bibliography

[1] M. Shur, *Solid-State Electron.* **42**, 2119 (1998).

[2] M. Razeghi, A. Rogalski, *J. Appl. Phys.* **79**, 7433 (1996).

[3] C. Jacoboni and L. Reggiani, *Reviews of Modern Physics*, **55**, 645 (1983).

[4] C. Sevik and C. Bulutay *IEE Proc.-J: Optoelectron.* **150**, 86 (2003).

[5] C. Sevik and C. Bulutay *Appl. Phys. Lett.* **83**, 1382 (2003).

[6] M. Lundstrom, *Fundamentals of Carrier Transport*, 2nd ed. (Cambridge University Press, 2000).

[7] K. Tomizawa, *Numerical Simulation of submicron Semiconductor Devices* (Artech House, 1993).

[8] C. Sevik and C. Bulutay, to be published in *Semicond. Sci. Technol.*

[9] G. Lehmann and M. Taut, *Phys. Status Solidi B* **54**, 469 (1972).

[10] D. K. Ferry, *Semiconductor Transport* (Taylor and Francis, 2000).

[11] A. D. Boardman (editor), *Physics Programs* (Wiley, 1980).

[12] C. Bulutay, *Semicond. Sci. Technol.* **17**, L59 (2002).

[13] W. Fawcett, A. D. Boardman andS. J. Swain, *Phys. Chem. Solids* **31**, 1963 (1970).

[14] C. Bulutay, B. K. Ridley, and N. A. Zakhleniuk, *Phys. Rev. B* **62**, 15754 (2000).

[15] C. Bulutay, B. K. Ridley, and N. A. Zakhleniuk, *Physica B* **314**, 63 (2002).

[16] M. Farahmand, C. Garetto, E. Bellotti,K. F. Brennan, M. Goano, E. Ghillino, G. Ghione, J. D. Albrecht and P. P. Ruden, *IEEE Trans. Electron Devices* **48**, 535 (2001).

[17] M. V. Fischetti and S. E. Laux, *J. Appl. Phys.* **80**, 2234 (1996).

[18] K. Tomizawa, Y. Awano, N. Hashizume and M. Kawashima, *IEE Proc.* **129**, 131 (1982).

[19] P. Lugli and D. K. Ferry *IEEE Trans. Electron Devices* **32**, 2431 (1985).

[20] M. Razeghi, Proc. IEEE **90**, 1006 (2002).

[21] A. Osinsky, M. S.Shur, R. Gaska, and Q. Chen, *Electron. Lett.* **34**, 691 (1998).

[22] K. A. McIntosh, R. J. Molnar, L. J. Mahoney, A. Lightfoot, M. W. Geis, K. M. Molvar, I. Melngailis, R. L. Aggarwal, W. D. Goodhue, S. S. Choi, D. L. Spears, S. Verghese, *Appl. Phys. Lett.* **75**, 3485 (1999).

[23] J. C. Carrano, D. J. H. Lambert, C. J. Eiting, C. J. Collins, T. Li, S. Wang, B. Yang, A.L. Beck, R.D. Dupuis, J. C. Campbell, *Appl. Phys. Lett.* **88**, 924 (2000).

[24] B. Yang, T. Li, K. Heng, C. Collins, S. Wang, J. C. Carrano, R. D. Dupuis, R. C. Campbell, M. J. Schurman, and I. T. Ferguson, *IEEE J. Quantum Electron.* **36**, 1389 (2000).

[25] P. J. Hambleton, S. A. Plimmer, J. P. R. David, G. J. Rees, and G. M. Dunn, *J. Appl. Phys.* **91**, 2107 (2002).

[26] K. F. Li, D. S. Ong, , J. P. R. David, G. J. Rees, R. C. Tozer, P. N. Robson, and R. Grey, *IEEE Trans. Electron Devices* **45**, 2102 (1998).

[27] G. M. Dunn, G. J. Rees, J. P. R. David, S. A. Plimmer, and D. C. Herbert, *Semicond. Sci. Technol.* **12**, 111 (1997).

[28] F. Ma, S. Wang, X. Li, K. A. Anselm, X. G. Zheng, A. L. Holmes, and J. C. Campbell, *J. Appl. Phys.* **92**, 4791, (2002).

[29] D. Vasileska and S. M. Goodnick, *Mat. Sci Eng. R* **38**,181 (2002).

[30] B. K. Ridley, *Quantum Processes in Semiconductors*, 4th ed. (Oxford University Press, 1999).

[31] K. Kunihiro, K. Kasahara, Y. Takahashi, and Y. Ohno, *IEEE Electron Device Lett.* **20** 608 (1999).

[32] M. A. Osman and D. K. Ferry, *Phys. Rev. B* **36**, 6018 (1987).

[33] M. V. Fischetti and J. M. Higman, *Monte Carlo Device Simulation: Full Band and Beyond*, edited by K. Hess (Kluwer, 1991).

[34] İ. H. Oğuzman, J. Kolnik, and K. F. Brennan, *J. Appl. Phys.* **80**, 8 (1996).

[35] R. W. Hockney and J. W. Eastwood, *Computer Simulation Using Particles*, (Institute of Physics, 1988).

[36] N. Balkan, B. K. Ridley, and A. J. Vickers (Editors) *Negative Differential Resistance and Instabilities in 2-D Semiconductors* (Plenum, 1993).

[37] M. Shur, *Introduction to Electronic Devices*, 1st ed. (Wiley, 1996).

[38] G. M. Dunn and M. J. Kearney *Semicond. Sci. Technol.* **18**, 794 (2003).

[39] E. Schöll, *Nonlinear Spatio-Temporal Dynamics and Chaos in Semiconductors* (Cambridge University Press, 2001).

[40] K. Oshio and H. Yahata *J. Phys. Soc. Jpn.* **64**, 1823 (1995).

[41] K. Hess, *Advanced Theory of Semiconductor Devices* (Prentice Hall, 1998), 207.

[42] V. Gruzinskis, E. Starikov, P. Shiktorov, L. Reggiani, and L. Varani *J. Appl. Phys.* **76**, 5260 (1994).

[43] R. P. Joshi, S. Viswanadha, P. Shah, and R. D. del Rosario *J. Appl. Phys.* **93**, 4836 (2003).

[44] A. Di Carlo, P. Lugli, C. Canali, R. Malik, M. Manfredi, A. Neviani, E. Zanoni, and G. Zandler *Semicond. Sci. Technol.* **13**, 858 (1998).

[45] M. V. Fischetti, J. M. Higman, in: Hess K (Ed.) *Monte Carlo Device Simulation: Full Band and Beyond*(Kluwer, 1991), 123.

[46] M. Reigrotzki, M. Dür, W. Schattke, N. Fitzer, R. Redmer, and S. M. Goodnick *Phys. Stat. Sol.* **204**, 528 (1997).

[47] Y. Ando, W. Contrata, N. Samoto, H. Miyamoto, K. Matsunaga, M. Kuzuhara, K. Kunihiro, K. Kasahara, T. Nakayama, Y. Takahashi, N. Hayama, and Y. Ohno *IEEE Trans. Electron Devices* **47**, 1965 (2000).

[48] M. Farahmand and K. F. Brennan *IEEE Trans. Electron Devices* **46**, 1319 (1999).

[49] H. K. Jung, H. Nakano, and T. Taniguchi *Physica B* **272**, 244 (1999).

[50] O. Mouton, J. L. Thobel, and R. Fauquembergue *J. Appl. Phys.* **81**, 3160 (1997).

[51] J. Bude and K. Hess *J. Appl. Phys.* **72**, 3554 (1992).

[52] K. Yeom, J. M. Hinckley, and J. Singh *J. Appl. Phys.* **80**, 6773 (1996).

[53] H. Ito and Y. Ueda *Phys. Lett. A* **280**, 312 (2001).

[54] M. V. Fischetti and S. E. Laux, *Phys. Rev. B* **38**, 9721 (1988).

Appendix A

Impact ionization and alloy scattering

In this appendix, we would like to explain our approach for the impact ionization (II) and alloy scattering in more detail for documentation purposes.

A.1 Impact ionization

The only available experimental report about II relevant to our work is on GaN by Kunihiro *et al.* [31]. Using our EMC framework, we are able to fit to their electron ionization coefficient with an II scattering rate of P_{II}^{GaN}(1/s)=2.5 $\times$ 10^{16} (E_{in} - E_{th}^{GaN} $)^8$ $u(E_{in}$ - $E_{th}^{GaN})$, where E_{in} is the energy of the electron in eV, E_{th}^{GaN}= 4 eV is the II threshold energy, and $u(\cdot)$ is the unit step function[1]. This expression, when compared to the *ab initio* results for GaN [46] possesses similar exponent and threshold values, but a reduced coefficient. On the other side, for $Al_xGa_{1-x}N$ Ando *et al.* [47]. used linear interpolation between the II rates of GaN and AlN, assuming for simplicity a null value for AlN. Aiming for a more realistic estimation for AlN, we make use of the Keldysh approach valid for parabolic bands while Bloch overlaps are taken into account via the f-sum rule

[1]The contents of this chapter has been adopted from Ref [12].

Table A.1: Band edge analysis throughout the lowest two conduction bands of $Al_xGa_{1-x}N$ alloys: band edge energy, E, density of states effective mass, m^*, and non-parabolicity factor, α (other than the lowest valley, two-band $\vec{k} \cdot \vec{p}$ values are preferred). Equivalent valley multiplicities, N_v are included as well. Note that the ordering of the U and K valleys is interchanged at an aluminium mole fraction of 0.6.

E(eV) m^*/m_0 α(eV^{-1})	GaN	$Al_{0.2}Ga_{0.8}N$	$Al_{0.4}Ga_{0.6}N$	$Al_{0.6}Ga_{0.4}N$	$Al_{0.8}Ga_{0.2}N$	AlN
$\Gamma_1(N_v = 1)$	0	0	0	0	0	0
	0.2	0.214	0.227	0.238	0.246	0.26
	0.262	0.243	0.230	0.221	0.213	0.207
$U(N_v = 6)$	1.34	1.285	1.233	1.181	1.131	1.05
	0.442	0.456	0.468	0.486	0.487	0.495
	0.064	0.056	0.049	0.043	0.039	0.035
$K(N_v = 2)$	1.59	1.444	1.307	1.179	1.057	0.9
	0.47	0.477	0.483	0.478	0.488	0.488
	0.055	0.050	0.045	0.042	0.039	0.106
$M(N_v = 3)$	1.87	1.830	1.798	1.769	1.741	1.68
	0.565	0.577	0.590	0.604	0.617	0.629
	0.035	0.030	0.026	0.023	0.020	0.017
$\Gamma_3(N_v = 3)$	2.14	2.23	2.312	2.390	2.462	2.49
	0.439	0.463	485	0.507	0.529	0.55
	0.056	0.046	0.039	0.032	0.027	0.023
Free electron band ($N_v = 1$)	3.5	3.6	3.7	3.8	3.9	4
	1	1	1	1	1	1
	0	0	0	0	0	0

Table A.2: A and K values in the electron II coefficient expression, $A\exp(-K/F)$, where, F is the electric field. A temperature of 300 K and an ionized impurity concentration of 10^{17} cm^{-3} are used.

	GaN	$Al_{0.2}Ga_{0.8}N$	$Al_{0.4}Ga_{0.6}N$	$Al_{0.6}Ga_{0.4}N$	$Al_{0.8}Ga_{0.2}N$	AlN
$A(10^7$ cm$^{-1})$	1.1438	1.5126	2.0647	1.7974	1.2993	8.8750
K(MV cm^{-1})	23.8933	31.6707	36.6251	37.7751	36.3373	37.5904

[10]. The corresponding II scattering rate comes out as $P_{II}^{AlN}(1/s)=7.04\times10^{11}$ $(E_{in}$ - E_{th}^{AlN} $)^2$ $u(E_{in}$ - $E_{th}^{AlN})$, where $E_{th}^{AlN}=6.84$ eV. Examining the forms of these two scattering rate expressions, we see that GaN possesses a soft threshold, whereas the Keldysh treatment demands a hard threshold for AlN. The latter should not be undermined as well, as Hess pointed out, the Keldysh approach can still adequately represent the experimental data for the case of steady-state phenomena [36].

Utilizing the results of first-principles characterization by Jung *et al.* on II [49], we employ a piecewise linear functional relation between the initial (E_{in}) and final (E_{fin}) energies of the impacting electron, measured from the conduction band minimum, as

$$E_{fin}=\begin{cases}0, & E_{in}<E_{th}^{AB}\\ c_1(E_{in}-E_{th}^{AB}), & E_{th}^{AB}\leq E_{in}\leq E_{br}^{AB}\\ c_2(E_{in}-E_0^{AB}), & E_{br}<E_{in},\end{cases}\tag{A.1}$$

where E_{br}^{AB} $=c_3E_{gap}^{AB}$, $E_0^{AB}=[c_1E_{th}^{AB}+(c_2-c_1)E_{br}^{AB}]/c_2$,and E_{br}^{AB} is the alloy II threshold energy obtained using Vegard's Law from the binaries The energy coefficients above, c_1, c_2 and c_3, are practically taken to be material independent [50], and we use the values of Jung *et al.* 's c_1=0.55, c_2=0.267, c_3=2.11 values extracted from GaAs data at 300 K [14], Fig. A.1. Incorporating the first-principles II scattering rate expression of this reference to our EMC formalism yields excellent agreement with the experimental results for GaAs [31], giving confidence on the validity of this approach. In bipolar simulations, such as APDs, it becomes important to include the secondary electron-hole pair as well. Their energies

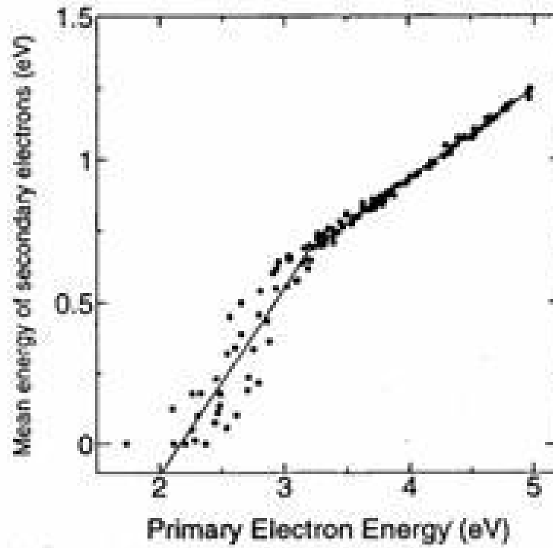

Figure A.1: Electron II coefficient versus inverse electric field. Dotted lines indicate the results when alloy scattering is not included, after Jung [49].

and momenta should be assigned in such a way to meet conservation laws as much as possible; more vital is the momentum conservation for the current gain considerations.

Returning to the $Al_xGa_{1-x}N$ system, electron II coefficient, , for several alloy compositions are plotted in Fig. A.2 with respect to electric field, F. These results are obtained for a temperature of 300 K and an ionized impurity concentration of 10^{17} cm^{-3}. We note that these curves do not obey Wolff's form, $A\ \exp(-K/F^2)$, but rather can be faithfully represented using Shockley's form of $A\ exp(-K/F)$; refer to Table A.1 for a listing of these constants, A and K. In this connection, we find it useful to add Bude and Hess's remark that the functional dependence of on F is closely related to the rise of density of states in the most important energy range, and not as much on the question of whether lucky electrons are important for the ionization or not [51].

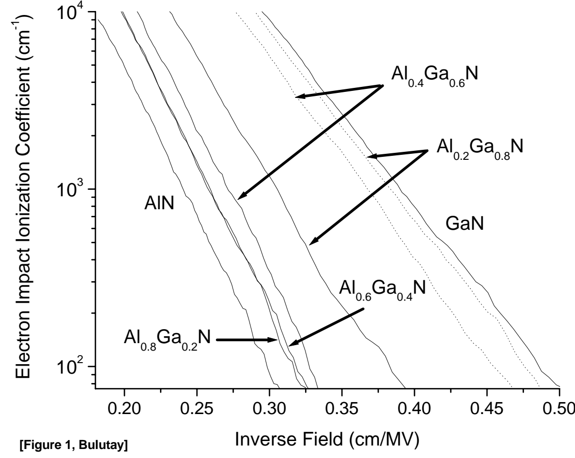

Figure A.2: Electron II coefficient versus inverse electric field. Dotted lines indicate the results when alloy scattering is not included. The curves for $Al_{0.6}Ga_{0.4}N$ and $Al_{0.8}Ga_{0.2}N$ merge at higher fields. These results are obtained for a temperature of 300 K and an ionized impurity concentration of 10^{17} cm^{-3}.

A.2 Alloy scattering

In a semiconductor alloy, the scattering of free carriers due to deviations from the virtual crystal model, as also employed in this work, has been termed as alloy scattering [10]. Recently, Farahmand and Brennan addressed alloy scattering in group-III nitride ternary alloys, using the conduction band offset between the binaries as the alloy potential [16]. They have argued that this approach yields an upper bound for alloy scattering. As a representative value, in our work we use $U_{alloy} = 0.91$ eV, which is half of the corresponding GaN/AlN conduction band offset. The dotted curves in Fig. A.2 corresponding to aluminium mole fractions of 0.2 and 0.4 indicate that when alloy scattering is turned off II is significantly enhanced. In contrast, the elastic nature of the alloy scattering might initially suggest a marginal effect on the electron energy distribution. However, the deviation of the electron wave vector away from the electric field due to an elastic scattering causes deceleration in the drift cycles, hence a loss in its energy of such an electron, lowering its potential for II. Fig. A.3 illustrates this point for

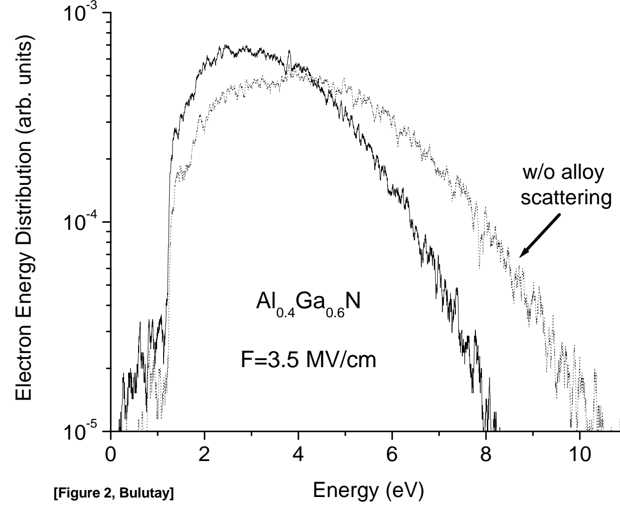

Figure A.3: Electron energy distribution for $Al_{0.4}Ga_{0.6}N$ at an electric field of 3.5 MV/cm, with (solid) and without (dotted) the alloy scattering. A temperature of 300 K and an ionized impurity concentration of 10^{17} cm^{-3} are considered

$Al_{0.4}Ga_{0.6}N$ (which is an important alloy composition for solar-blind applications) at an electric field value of 3.5 MV/cm; the depletion of the high energy tail of the distribution function due to alloy scattering explains the decrease in the II coefficient obtained in Fig. A.2. However, we would like to draw attention to two simplifications in our approach inherited from the treatment of Fischetti and Laux [17]. The alloy scattering is implemented as an intravalley process due to its small wavelength attenuation [17]; in the case of closely located valleys, like U and M, this may become rather crude. More importantly, the distribution of the final scattering angles is assumed to be isotropic, even though at higher energies alloy scattering attains a forward directional character [52]. Thus, we are lead to think that the effect of the alloy scattering may still be somewhat overestimated.